Journal of Materials Processing Tech. 316 (2023) 117917

Contents lists available at ScienceDirect

Journal of Materials Processing Tech.

journal homepage: www.elsevier.com/locate/jmatprotec

A novel hydraulic bulge test in hot forming conditions

A. Boyer [a,b], N. Demazel [a], J. Coër [c], M. Carin [a], H. Laurent [a,*], M.C. Oliveira [b]

[a] Univ. Bretagne Sud, UMR CNRS 6027, IRDL, F-56100 Lorient, France
[b] CEMMPRE, Department of Mechanical Engineering, University of Coimbra, Polo II, Rua Luís Reis Santos, Pinhal de Marrocos, 3030-788 Coimbra, Portugal
[c] NAVAL GROUP - Lorient, Avenue de Choiseul, F-56311 Lorient, France

ARTICLE INFO

Associate Editor: Zhenshan Cui

Keywords:
Hydraulic bulge test
Hot stamping
Heat treatable steel
Formability test
High temperature

ABSTRACT

A novel hydraulic bulge test device was developed to evaluate high temperature biaxial stress–strain curves of quenchable boron steel sheets. The work mainly focuses on the resistance heating designed to assure a homogeneous temperature field in the dome area of the circular blank where the hydraulic pressure will be applied. The practical hot stamping conditions, including the heating and cooling steps, were reproduced to perform hydraulic bulge tests on the Usibor®1500P steel for a temperature range between 700 to 900 °C, after an austenization step at 900 °C. Stress–strain curves were obtained from these expansion tests using the data extracted with a laser profilometer, due to the difficulties associated with the use of Digital Image Correlation at such high temperatures. Although the profilometer is a compromise solution, the comparisons between tensile and biaxial stress–strain results enable to verify the feasibility of the new device for the evaluation of the stress–strain curves at a high temperature in a biaxial state. The results point-out that, besides the difficulties with the acquisition of the strain fields and in the strain-rate control, there are also challenges in the interpretation of the metallurgical evolutions that can occur during the tests, which can affect the biaxial flow curves.

1. Introduction

In order to provide flow stress curves and forming limits for hot steel metal forming simulations up to high strain levels, knowledge of the thermo-mechanical behaviour of the materials is of the up-most importance. The mechanical properties of boron alloy steels after forming at elevated temperatures were studied by many researchers. Karbasian and Tekkaya (2010) showed the potential of the hot stamping procedure by summarizing the thermal, mechanical and microstructural aspects of this material and gave the technological aspects of the procedure. Merklein and Lechler (2006) reported the flow stress of hot-stamped 22MnB5 steels and its dependency on temperature in uniaxial tensile conditions. Li et al. (2019) developed a procedure for the constitutive parameters identification for boron steels under hot conditions, based on Digital Image Correlation (DIC) assisted tensile tests. However, the information on properties obtained at elevated temperatures under biaxial stress state, using the hydraulic bulge test on this kind of materials is very limited.

As shown by Lăzărescu et al. (2011), the biaxial bulge test under hydraulic pressure, enables the determination of the flow stress curves of sheet metals up to high strain levels before the occurrence of necking and fracture. Therefore, as studied by Bleck and Blumbach (2005), it enables the definition of the hardening behaviour up to large plastic deformations, when compared with the ones attained in the uniaxial tensile test. Koç et al. (2011) showed also that the biaxial stress mode is also very interesting because it is the major deformation mode in many sheet forming processes. In this context, Alharthi et al. (2018) used the hydraulic bulge test to obtain the value of one of the key material parameters required to define most advanced yield functions, the biaxial yield stress. Finally, this test provides a way to obtain the expansion mode of the Forming Limit Diagram (FLD), as for example in the work of Wu et al. (2016).

In the hydraulic bulge test, the sheet (square or circular) is clamped between a circular die and a blank-holder, as shown in Fig. 1. When a pressure p is applied to the fluid in the lower chamber, the sheet is bulged into the cavity of the die. ISO16808 (2014) standard recommends that the ratio between the sheet thickness, t, and the die diameter, D, to be equal to or lower than 1/33. The clamping force between the die and the blank-holder has to be high enough to prevent the sliding of the sheet to the die cavity. Therefore, sometimes a drawbead is used to prevent the movement of the sheet in the clamped region, as shown by Kaya et al. (2008). The advantage of this test when compared to the Nakazima or Marciniak tests is that the sheet is formed into a hemispherical geometry without using a punch. Thus, the deformation is not affected by friction. These tests are used to evaluate the materials formability while the bulge test enables also the evaluation of the stress–strain curves.

Several hydraulic bulge tests devices have been developed during the last twenty years to perform the analysis in warm and hot conditions. Most of these devices were developed to test lightweight alloys,

* Corresponding author.
E-mail address: herve.laurent@univ-ubs.fr (H. Laurent).

https://doi.org/10.1016/j.jmatprotec.2023.117917
Received 28 October 2022; Received in revised form 3 February 2023; Accepted 14 February 2023
Available online 4 March 2023

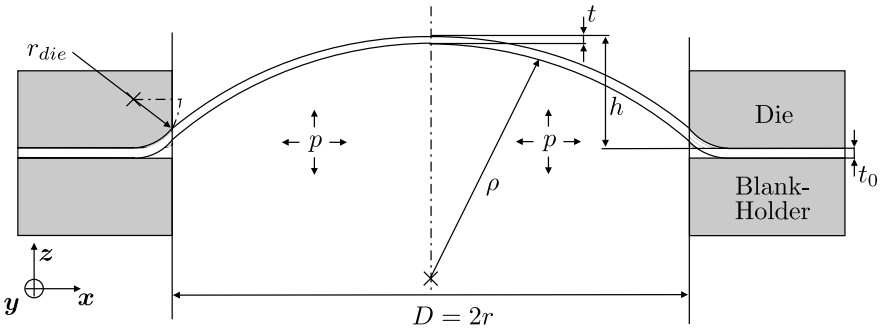

Fig. 1. Principle of the biaxial bulge test (adapted from Lafilé et al., 2021) and dimensional parameters used in this study (cross-sectional view).

such as aluminium and magnesium alloys, in warm conditions. The heating technologies typically used to reach temperatures inferior to 600 °C are hot oil bath, cartridge heaters and furnaces. Lee et al. (2013) proposed a testing device for temperatures up to about 125 °C where only the oil is heated. In Ayres and Wenner (1979), samples of AA5182-O aluminium alloy were tested while submerged in a hot circulating oil bath, whereas the tools were heated by cartridge heaters, up to a temperature of 200 °C. In other studies, the die, blank-holder and blank were all submerged in a liquid, heated by cartridge heaters installed in various locations inside the tools. For example, Kaya et al. (2008) conducted tests on the AZ31-O magnesium alloy for temperature up to 225 °C. Groche et al. (2002) conducted tests on the EN AW-5083 and EN AW-6016 alloys with temperatures up to 250 °C and determined the biaxial flow stress curves for these materials. Using the same principle, other researchers explored the biaxial hydraulic bulge tests at warm temperatures. In Koç et al. (2011), the AA5754 aluminium alloy was studied, for a maximum temperature of 260 °C, while in Mahabunphachai and Koç (2010) two aluminium alloys: AA5052 and AA6061, were studied up to 300 °C. Li and Ghosh (2004) studied the biaxial warm forming behaviour of three automotive aluminium sheet alloys for a temperature range between 200 and 350 °C. To obtain the FLD of these alloys, the tools were heated using embedded heaters while the blank was heated by convection. Using the same principle, the formability of the AA5083 alloy was tested at 550 °C by Banabic et al. (2005), under a constant strain rate, by controlling the bulging gas pressure, for circular and elliptical dies and by the cone-cup testing method.

Abu-Farha and Hector (2011) developed a pneumatic stretching test where the forming die assembly is placed in a heating chamber. They explored sheet orientation effects on the hot formability limits of two lightweight materials: the AA5083 aluminium and the AZ31B magnesium alloys, up to 450 °C. Liu et al. (2015) used a resistance furnace to heat the tools and sample to determine the hardening curves of an AA7075 sheet, for temperatures lower than 280 °C. Shao et al. (2018) determined the FLDs for an AA5754 alloy at various temperatures (200 to 300 °C) and forming speeds (20 to 300 mm s^{-1}) by setting up the test tool in a hot furnace, to create an isothermal environment.

Concerning temperatures higher than 600 °C, furnaces are still used but induction and resistance heating methods are emerging. For example, Bariani et al. (2008) presented a stretching-forming Nakazima test, for evaluating the formability limits in the hot stamping of high strength steels, for temperatures up to 700 °C. In this case, the metal blanks and the tools are heated by induction. Shao et al. (2016) used a resistance heating method, to develop a novel biaxial testing system in a Gleeble testing machine based on a type of cruciform specimen to evaluate the forming limits under hot stamping conditions for boron steel and AA6082 aluminium alloys. Li et al. (2012) evaluated the effect of applying a pulse current to heat a rectangular sheet by developing a free bulging test that was applied to AZ31 Mg alloy at 400 °C. With the same heating method, Wang et al. (2018) studied the superplastic gas bulging of Ti_2AlNb alloy at 980 °C. Finally, by using resistance heating by Joule effect of a rectangular sheet, an hot-gas-bulge test was designed by Braun et al. (2016) to characterize hot stamping steel 22MnB5, at temperatures up to 900 °C and strain rates up to 0.5 s^{-1}.

This resistance heating technique (or conduction heating), as proposed by Mori et al. (2017), is a very attractive method to heat a thin metallic sheet. Resistance heating is a promising alternative to roller-hearth furnaces, which are commonly used for hot stamping since it provides very high heating rates, as shown by Mori et al. (2020). If the output of the power supply is sufficient, Maeno et al. (2019) showed that it is a very attractive way for heating sheets while avoiding metallurgical modifications (like oxidation and decarburization) in the case of heat-treatable materials. Additionally, resistance heating seems more suitable to use an optical measurement device, than a furnace or an inductor. However, the temperature distribution in the heated specimen is in general less homogeneous, when compared to a specimen which is heated by a furnace, as was observed by Braun et al. (2014b). Indeed, Liang et al. (2014) noticed that if the blank has a variable current cross section, then the temperature field can be heterogeneous with severe overheatings.

The Joule heating process is already used in industry, but often only applied to blanks with long and narrow geometry, such as: rectangular blanks studied by Mori et al. (2005) for ultra-high strength steels, and by Maeno et al. (2018), for hot stamping steel; pipes, rods, wires by Kolleck et al. (2008); and L-angle profiles by Deng et al. (2018). This technique was also used by Nakagawa et al. (2020) for non-rectangular steel sheets by local preheating and in the hot stamping of a front bumper by Liang et al. (2021). Demazel et al. (2021) adapted this technology to any blank shape, as exemplified for a windscreen upright blank, by splitting it into several rectangular strips heated by five electrical generators. Santos et al. (2014) used also this method to assist the friction stir welding.

During the bulge test, the temperature field in the blank should be as uniform as possible, because the objective is to determine the stress–strain relationship in biaxial state at high, constant, temperatures. In this case, there are also challenges related with the measurement of the evolution of the bulge radius and polar thickness of the specimen. Nowadays, the DIC technique is classically adopted for strain measurement during bulge tests, as mentioned by Mulder et al. (2015). DIC enables full-field strains to be measured at different stages of forming by comparing the digital images of a pattern sprayed or a grid etched on the specimen, even for temperatures up to 500 °C as used by Shao et al. (2016) or for very thin sheets by Sène et al. (2013). However, the use of high temperature conditions gives rise to difficulties when using DIC systems. Indeed, the pattern required for using this measurement method needs to withstand high temperature and large stretching, without sliding or cracking. Thus, currently, the DIC at very high temperature and under large deformation conditions remains difficult to control, as mentioned in Aksenov and Sorgente (2020). Thus, an alternative technique, using a laser profiler is tested in this work, as already done by our team in Boyer et al. (2019), to obtain the stress–strain curve from a biaxial test, for an AA6061-T6 aluminium alloy at 150 °C.

As other material characterization experiments, the bulge test might also be influenced by non-isothermal process conditions and deviations in the testing strain rates. Indeed, in the majority of the hydraulic bulge methods at high temperature presented before, direct measurements of the specimen pole temperature revealed non-isothermal condition during bulging, as in the work of Wang et al. (2010) and that it is difficult to maintain a constant strain rate during the experiment, as mentioned in Jocham et al. (2017). In fact, this difficulty is known since the early work of Jovane (1968) and some approaches have been proposed. In this context, Dutta and Mukherjee (1992) proposed an analytical equation to describe the evolution of pressure with time for the bulge test. Banabic et al. (2005) used this equation to describe the free bulging stage of the test performed with a conical die. In this work, the authors also proposed analytical pressure–time evolutions for bulging with circular and elliptic dies. More recently Suttner and Merklein (2016) suggested using strain control with DIC system.

If the extent of these non-perfect process conditions is significant, Braun et al. (2014a) proposed to determine the biaxial flow curve by inverse modelling. Aksenov and Sorgente (2020) used in their work, a double-step numerical procedure that allowed them to calculate the stress–strain curves for constant strain rates, in the case of a superplastic Alnovi-U aluminium alloy in conditions of biaxial tension at 500 °C.

In summary, there are three major challenges in the acquisition of the biaxial stress–strain curves from hydraulic bulge tests, at high temperature: (i) a heating method that assures a homogeneous temperature field in the dome area; (ii) a procedure that enables the measurement of curvature and thickness (or principle strains) evolutions at the pole; and (iii) a procedure to assure a constant strain rate in the dome area during bulging. In this work, an additional challenge is addressed: reproducing industrially relevant hot forming conditions for the boron steel Usibor®1500P, which includes heating at 900 °C to ensure a complete austenization, as highlighted in Venturato et al. (2017). Therefore, it is mainly focused on the development of a direct resistance heating technology, by Joule effect, applicable to circular blanks. As previously mentioned, Joule effect heating is easily achievable for a rectangular sheet, it is quite challenging to establish a method allowing rapid and homogeneous heating of a circular blank. The isolated metal tools required to clamp the blank lead also to thermal conduction, which introduce a radial thermal gradient. Thus, the challenge of using Joule effect heating is to obtain a uniform temperature field on the blank area where the hydraulic pressure will be applied. This is particularly difficult when considering hot forming conditions such as those used for boron steels, due to the high temperature required. Therefore, a numerical thermoelectric model from COMSOL Multiphysics® was built to help establishing the conditions for the heating procedure to be adopted. This model was also applied to enable the control of the temperature throughout the duration of the test. Thus, unlike other types of resistance heating systems in bulge apparatus (*e.g.* Braun et al. 2016, 2014b), it is possible to adjust and control the temperature of the blank during the forming step. Moreover, it is possible to reproduce hot stamping conditions by controlling the heating rate, soaking time and pressure rate.

The remainder of the manuscript is organized as follows. Section 2 presents the chemical composition of the 22MnB5 alloy and the thermal properties required for the development of the numerical resistance heating model. In Section 3, the COMSOL Multiphysics® thermoelectric model is described and used to establish a configuration that enables heating of the circular blank in the hydraulic bulge test. Then, the experimental set-up is described. A comparison between experimental and numerical temperature distributions during the heating phase is presented in order to validate the heating solution proposed. In Section 4, the methods used to extract the stress–strain curves from expansion and uniaxial tensile tests are presented. A subsection is devoted to the many difficulties encountered in applying DIC techniques, which justify the adoption of a laser profilometer as a compromise alternative. Note that, the comparison of results obtain with DIC and the laser profilometer was previously reported by our team in Boyer et al. (2019), for an AA6061-T6 aluminium alloy at 150 °C. The aim of this subsection is to systematize the issues that need further improvements, in order to be able to apply DIC techniques at high temperatures. The biaxial stress–strain curves of the Usibor®1500P are compared with the ones obtained using tensile tests on a Gleeble machine in Section 5. This section includes some explanations for the differences observed in the results obtained under tensile and biaxial conditions. Finally, the main conclusions are summarized in Section 6.

Table 1
Chemical composition (wt.%) of the Usibor®1500P steel.

C	Mn	B	Si	P	Cu	Ni	Cr	Al	Ti	Mo
0.22	1.23	0.004	0.25	0.008	0.03	0.02	0.20	0.03	0.037	< 0.02

2. Material

The boron/manganese micro-alloyed steel used in this study is an Usibor®1500P, produced by ArcelorMittal, with initial nominal thickness values of $t_0 = 0.9$ mm and $t_0 = 1.0$ mm. The chemical composition of this steel is given in Table 1.

The sheets of this quenchable steel are usually protected from oxidation and decarburization with an Al-Si layer, basically composed of 90% aluminium and 10% silicon. In this study, the sheets are covered with 80 g m^{-2} of Al-Si coating, *i.e.* the thickness layer is between 23 and 32 μm as mentioned in Demazel et al. (2018).

The steel thermal properties were obtained from the ArcelorMittal database (for further details refer to Demazel (2018)). The evolutions in function of temperature of the density ρ, the thermal conductivity k, the specific heat C_p, the electrical conductivity σ_e and the emissivity ε are presented in Fig. 2.

The density decreases with the increase of temperature, except for the small increase that occurs at the transformation temperature into austenite (≈ 730 °C). The thermal conductivity presents a strong decrease during the austenitization stage, but afterwards shows an increasing trend. The specific heat increases with temperature but suddenly, after the austenitization stage it decreases, due to the fact that this evolution takes into account the enthalpy of the phase transformation. As for many other metallic materials, the electrical conductivity decreases with the increase of temperature. The emissivity of the Usibor®1500P steel coated with the Al-Si layer depends on the alloying kinetic. It shows that the emissivity is low below 500 °C, decreases between 500 and 600 °C, and then increases for temperatures higher than 750 °C. For the electro-thermal model presented below, the emissivity is assumed as constant for temperatures higher than 900 °C. The decrease of the emissivity is due to the optical behaviour of the coating around 600 °C, since the blank surface appears as reflective as a mirror when the coating is melting. The increase after 750 °C is linked with the progress of the coating alloying to the steel surface, to form a protective layer against oxidation.

3. Design of the bulge test device

In order to have an uniform temperature field in the inner circular part of the blank, an electro-thermal coupled model, implemented in the finite element software COMSOL Multiphysics® was built to define the resistance heating system of the device. With this model, several parameters were tested and adjusted to attain a satisfactory configuration, such as the number, the shape, the position and the size of the electrodes, as well as the intensity and the time duration of the electrical current. The influence of the tools geometry on the cooling of the blank exterior perimeter and its effect on the temperature field in the central zone was also studied. The details about the numerical model are presented in this section. The integration of these numerical solutions in the new bulge test device is also described.

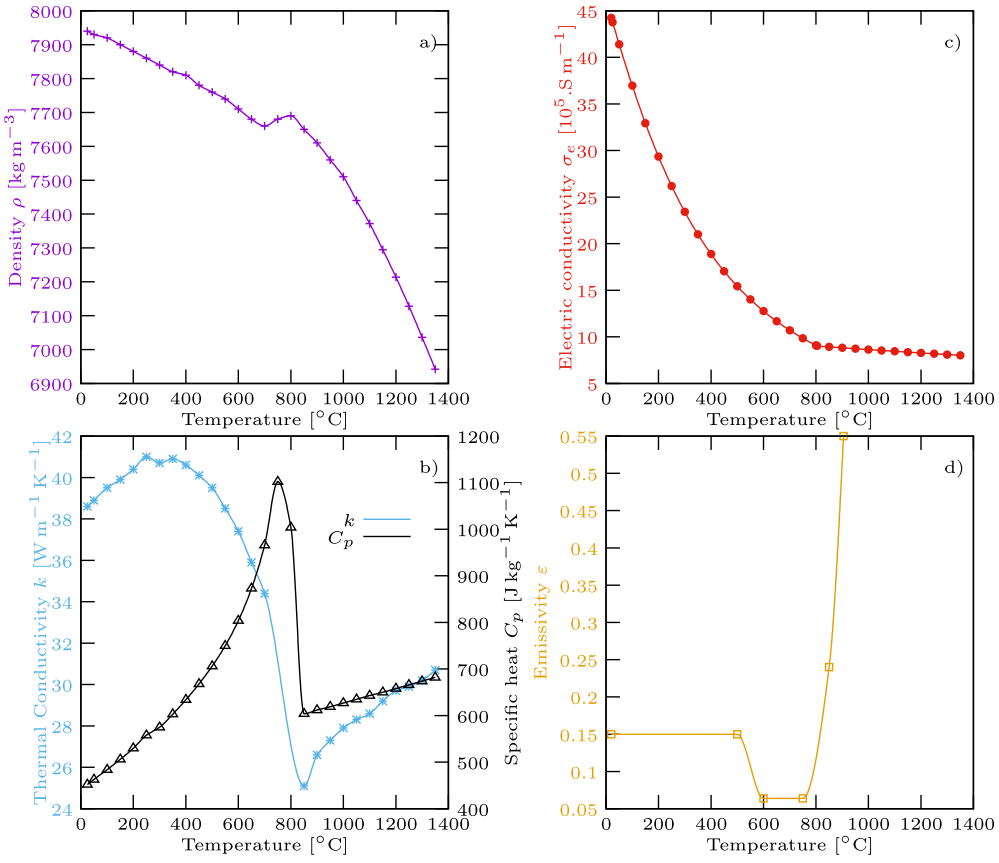

Fig. 2. Thermal properties: (a) Density ρ; (b) Thermal conductivity k and specific heat C_p; (c) Electrical conductivity σ_e and (d) Emissivity ε.

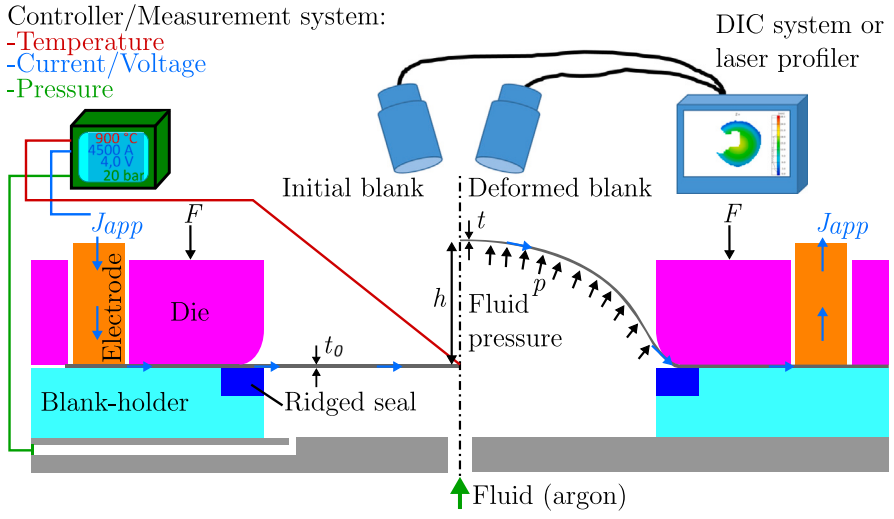

Fig. 3. Principle of the hydraulic bulge test device with pressure/electrical/temperature controller and DIC optical measurement system or laser profilometer.

3.1. Resistance heating design

The principle of the hydraulic bulging setup used in this study is shown in Fig. 3. This device is composed of a circular blank completely clamped on its perimeter between the die and the blank-holder. After the clamping, the blank is heated by Joule effect using electrodes and finally it is deformed by an inert pressured gas (argon). Both tools are supposed electrically isolated. The blank has an exterior diameter of 240 mm and the die diameter is $D = 2r = 120$ mm.

The geometry of the 3D electro-thermal model is composed of the blank, the tools (die and blank-holder) and the electrodes. The temperature dependence of the thermal parameters of the blank follows the evolutions presented previously in Fig. 2. The thermal problem is solved using the classical energy conservation law:

$$\rho(T)\, C_p(T)\, \frac{\partial T}{\partial t} = \mathrm{div}\left(\boldsymbol{k}(T)\ .\ \mathrm{grad}(T)\right) + Q_{Joule} \tag{1}$$

where $\boldsymbol{k}$ is the thermal conductivity tensor (considered isotropic), T is the temperature of the blank surface and Q_{Joule} is the heat source induced by the Joule effect given by:

$$Q_{Joule} = \mathrm{grad}^{\mathrm{T}}(V)\ .\ \boldsymbol{\sigma}_e(T)\ .\ \mathrm{grad}(V) \tag{2}$$

where σ_e is the electrical conductivity second order tensor (considered isotropic) and V is the electrical potential. The electrical problem is solved using the current continuity equation:

$$\mathrm{div}\,(\boldsymbol{J}) = 0 \tag{3}$$

where $\boldsymbol{J}$ represents the electrical current density vector, given by the local Ohm's law:

$$\boldsymbol{J} = \boldsymbol{\sigma}_e\,(T)\ .\ \mathrm{grad}\,(V) \tag{4}$$

Convective losses are described by the Newton law:

$$-\boldsymbol{n}\ .\ \boldsymbol{\varphi}_{conv} = h\left(T_{air} - T\right) \tag{5}$$

whereas radiative losses are described by the Stefan–Boltzmann law:

$$-\boldsymbol{n}\ .\ \boldsymbol{\varphi}_{rad} = \varepsilon\,(T)\ .\ \sigma_b\left(T_{ext}^4 - T^4\right) \tag{6}$$

where $\boldsymbol{n}$ is the unit normal vector to the blank's surface, $\boldsymbol{\varphi}_{conv}$ and $\boldsymbol{\varphi}_{rad}$ are the convective and radiative heat flux vectors, h is the heat transfer coefficient, $sigma_b$ is the Stefan–Boltzmann constant, T_{air} = 20 °C is the air temperature and T_{ext} = 20 °C is the temperature of the surrounding surface. These losses by radiation and convection are calculated assuming the blank as a grey body and constant convection heat transfer coefficients. The value used for h is assumed constant at 10 W m^{-2} K^{-1}.

A condition of electrical insulation is used between the tools and the external surfaces of the blank, such as:

$$-\boldsymbol{n}\ .\ \boldsymbol{J} = 0 \tag{7}$$

An input density current J_{app} is applied to the upper surfaces of the electrodes, as schematically illustrated in Fig. 3, such as:

$$-\boldsymbol{n}\ .\ \boldsymbol{J} = \pm J_{app} \tag{8}$$

The electrical current density between two surfaces in contact is evaluated by:

$$-\boldsymbol{n}\ .\ \boldsymbol{J}_{cont} = \frac{(V_1 - V_2)}{ECR} \tag{9}$$

where $\boldsymbol{J}_{cont}$ is the contact electrical density vector, ECR is the Electrical Contact Resistance coefficient and V_1 and V_2 are the electrical potentials of the two surfaces in contact.

The Joule effect due to the electrical contact resistance is taken into account with the following equations:

$$\begin{cases} -\boldsymbol{n}\ .\ \left(\boldsymbol{k}\ .\ \mathrm{grad}\left(T_1\right)\right) &= \dfrac{(T_2 - T_1)}{TCR} + (1-\alpha)\dfrac{(V_1 - V_2)^2}{ECR} \\ -\boldsymbol{n}\ .\ \left(\boldsymbol{k}\ .\ \mathrm{grad}\left(T_2\right)\right) &= \dfrac{(T_1 - T_2)}{TCR} + \alpha\dfrac{(V_1 - V_2)^2}{ECR} \end{cases} \tag{10}$$

where TCR is the Thermal Contact Resistance coefficient, T_1 and T_2 are the temperatures of each surface in contact and α is the partition coefficient with a chosen value of 0.5 due to the metallic contact, as described in the work of Rogeon et al. (2008).

The choice of ECR and TCR values is a particularly delicate point, since they depend on the contact conditions, such as the imperfections of rough surfaces and the contact pressure between the two surfaces. In the work of Blaise et al. (2013), the TCR, the latent heat of the austenite to martensite transformation and the Koistinen–Marburger parameters are evaluated by an inverse method using results of a contact heating device in order to improve the accuracy of numerical simulations of the hot stamping process. Pradille et al. (2010) showed that the ECR decreases with the increase of temperature or pressure. Terhorst et al. (2016) studied lubricant and metallic contacts using experimental and numerical analysis. Their model used for TCR and ECR takes into account many dependencies such as the real contact surface area, the contact temperature and the contact pressure.

The contact resistance coefficients were estimated in this study using a device similar to the one presented in Loulou et al. (2006). As described in Demazel (2018), a mean contact pressure between the electrodes and the blank of 0.5 MPa was applied and the values of ECR = 2.2 × 10^{-7} Ωm^2 and TCR = 6.5 × 10^{-4} K m^2 W^{-1} were estimated. These values were validated by comparing experimental with numerical results, when heating a rectangular blank in Demazel et al. (2021).

Concerning the type of finite elements, after a numerical convergence study, 3D tetrahedral elements with quadratic interpolation and average sizes of 7.4×10^{-5} m for the blank, and 3.3×10^{-2} m for the tools, lead to the best solutions. The maximum step time was set to 0.05 s.

In a preliminary study of Demazel et al. (2016), this electro-thermal model showed that the use of one pair of electrodes to heat a circular blank results in a heterogeneous distribution of the current flow, leading to an heterogeneous temperature field. According to the studies carried out at the Leibniz University, by Behrens et al. (2015), one of the solutions to heat uniformly a blank with a variable electrical current cross section is to use several pairs of electrodes. Therefore, several combinations were numerically tested using multi-electrodes combinations.

The solution that lead to an homogeneous temperature field in the centre of the blank was obtained by using three pairs of electrodes, oriented at 60° from each other, as shown in Fig. 4 (see also Demazel 2018). In this case, each pair of electrodes, as described in Fig. 5a, is activated alternately, by switching the pairs of electrodes in contact with the blank. After a pair of electrodes has been active for a defined period t_{app}, it is inactivated, while another pair supplies the power. This type of scheme for the electrical current application aims to uniformly heat the central area of the blank and reduce hot spots near the electrodes.

The influence of the electrodes geometry and their position in relation to the tools was also studied with the numerical model. These parameters mainly affect the hot spots in the areas of the blank around the electrodes. The temperature may become higher than 600 °C, which leads to the melting of the Al-Si coating and a consequent degradation of the electrodes. To avoid these hot spots, the electrodes must be located through the die to cool down the blank zones around the electrodes. After several numerical trials, a good solution was obtained with the geometry and the positions for the electrodes inside the tools, as shown in Fig. 4 (see Demazel (2018) for further details).

This configuration was used to study the influence of the electrical cycle on the heating time and the temperature field in the central area of the blank. As expected, the longer is the application time t_{app} and the higher is the electrical current intensity, the faster is the heating. However, despite the electrode position inside the tools, the electrical cycle has a considerable influence on the maximum temperature attained in the blank areas located around the electrodes. Moreover, to obtain a uniform temperature field in the centre of the blank, the application time t_{app} must be short, to have a rapid rotation of the electrical current, associated with the switching of the electrodes. Thus, to avoid hot spots and to assure temperature uniformity, it is necessary to find a compromise between the application time and the total heating time. This needs also to take into account the final temperature, which in case of boron steel is 900 °C.

Fig. 5b presents an example of the electrical current application proposed for a total heating time of 50 s. This heating cycle is composed of two phases: heating and holding. During the heating phase of 34 s the application time t_{app} is 1.4 s with a current intensity that starts at about 4800 A and decreases to 4000 A, which then remains constant 20 s. During the temperature holding phase, the current is maintained constant at about 4400 A and the application time t_{app} is reduced to 0.7 s in order to achieve a constant uniform temperature in the centre of the blank.

Fig. 5c shows the temperature field at the end of the heating cycle, showing that hot spots are avoided while a temperature of 900 °C is attained at the centre of the blank. A drop of 35 °C between the centre of the blank and the radius of 40 mm is observed therefore, it can be

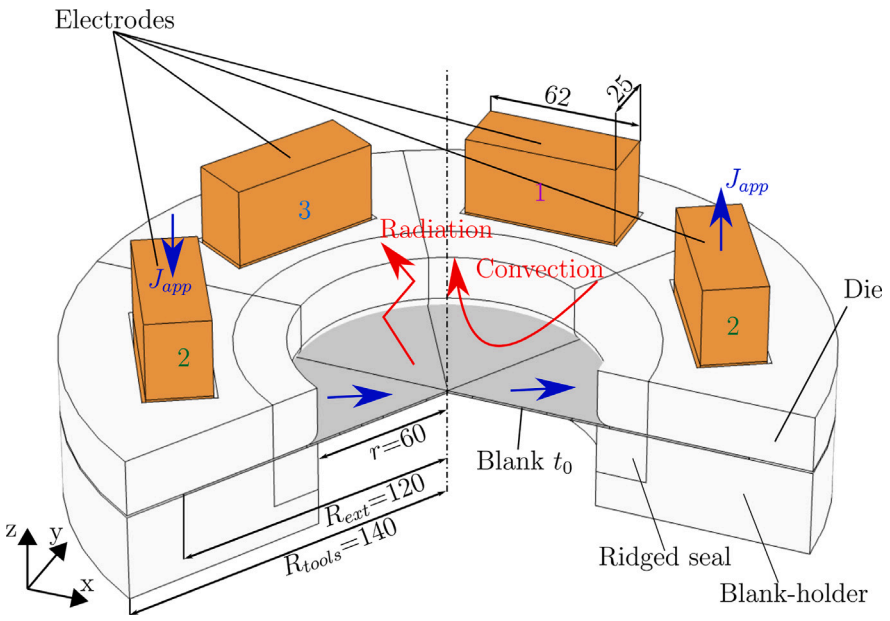

Fig. 4. Final geometry of the device defined using the 3D COMSOL Multiphysics® model with electro-thermal coupling (dimensions in mm).

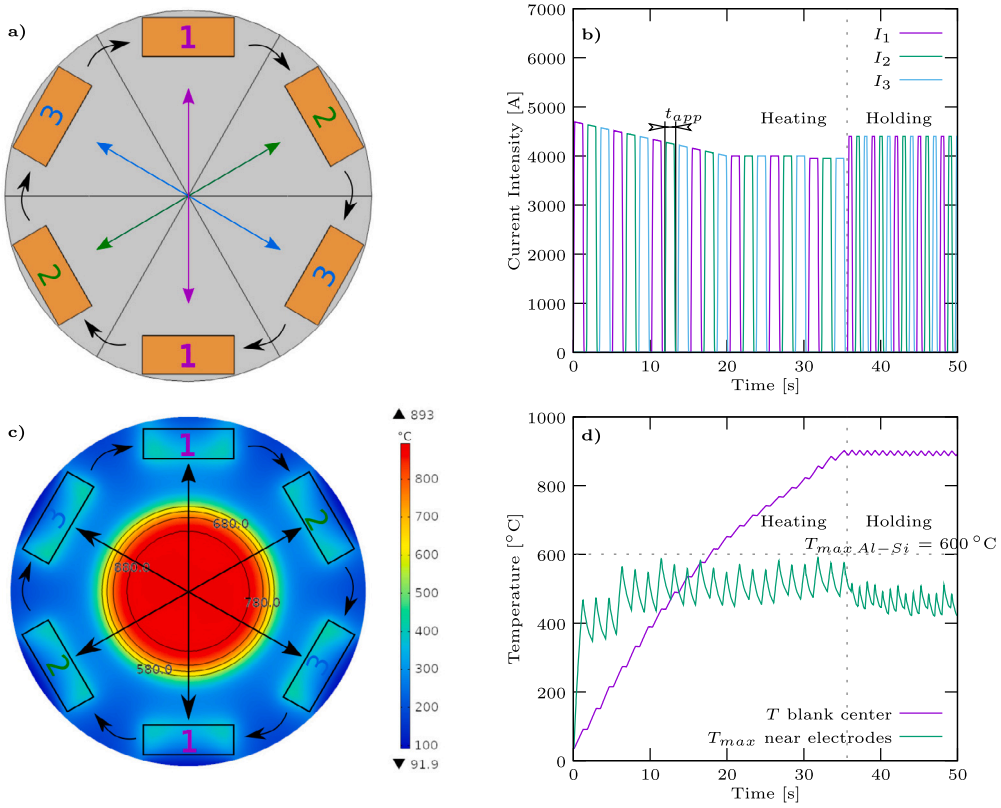

Fig. 5. (a) Schematic representation of the rotation of the electrical current in the three pairs of electrodes; (b) Example of an evolution of the electrical current intensity I, applied in each pair of electrodes, during a heating cycle of 50 s; (c) Temperature field resulting from the electrical cycle shown in (b) indicating the rotation motion of the electrodes; (d) Temporal evolution of the temperature at the centre of the blank and of the maximum temperature of the blank near the electrodes.

considered homogeneous in the central area, where the gas pressure will be applied. Circular isotherms are present due to the conduction cooling induced by the contact with the die and the blank-holder. Fig. 5d shows the evolution of the temperature at the centre of the blank as well as the maximum temperature near the electrodes resulting from the electrical cycle presented in Fig. 5b. The heating time to reached 900 °C is 35 s and the temperature of the hot spots of the blank around the electrodes is maintained under 600 °C.

In summary, the feasibility of resistance heating to attain a high temperature, constant in a bulge test device has been demonstrated using this numerical model. The temperature in the centre area of the blank proves to be fairly homogeneous, allowing to perform the

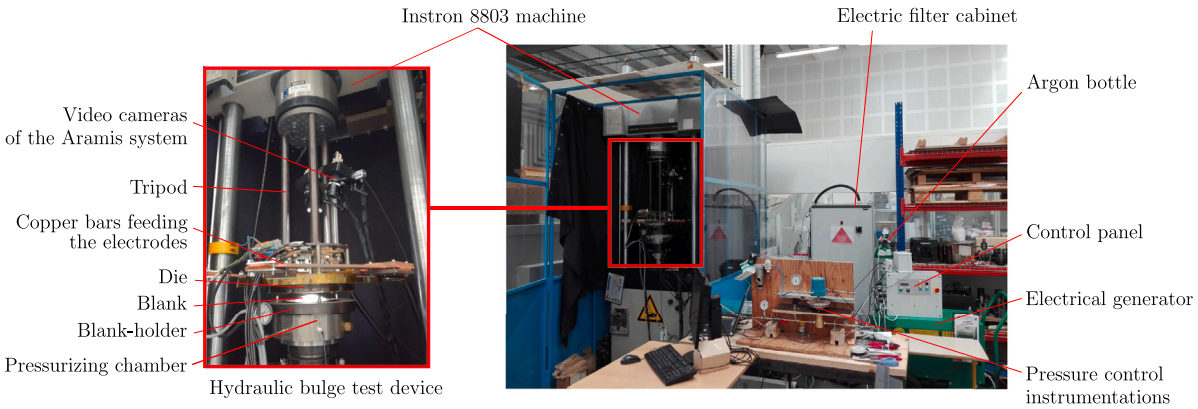

Fig. 6. Details of the hydraulic bulge test setup with the different components of the device.

expansion operation with a constant temperature in this area. In the following section, the expansion device developed taking into account these results will be presented in detail.

3.2. Experimental setup

Based on the numerical study previously presented, a bulge test device was designed and constructed. The different components of this device are presented in Fig. 6.

The device is composed of an electrical generator, which is supplied by two steps of the three-step network, in 400 V and 200 A, *i.e.* 80 kV A. The electrical generator can provide an alternative current with Root Mean Square (RMS) current up to 6000 A and a measured maximum power at the electrodes lower than 22 kW. It is associated with an harmonic filter cabinet, to reduce step imbalances resulting from the fact that the generator is supplied with two steps of the three-step network. The electrical current flow to the electrodes is ensured by a set of cables, blocks and braids in copper. A control panel commands the electrical current via a temperature control loop.

The test bench of the bulge-test, shown in the zoom of Fig. 6, is placed in an Instron 8803 tensile test machine, equipped with a load cell capacity of 500 kN. The tools are split into an upper (die) and a lower part (blank-holder), linked to the tensile machine with the help of a tripod. Both the die and the blank-holder are made of steel, coated with a non conductive film to electrically insulate them. An additional layer of Miglasil®, which is an electrical and thermal insulator, is added to improve the tools insulation.

At the beginning of the test, a compressive clamping force of 300 kN is applied to the sheet by the tensile machine. A steel ridged seal with a Klinger® flexible gasket assures the sealing of the pressure cavity (see Fig. 3). Double-acting pneumatic cylinders control each pair of electrodes, enabling the rotational permutation of the electrical field. A contact pressure of 0.5 MPa is applied successively between each electrode and the blank. A type *K* thermocouple with a diameter of 250 µm is welded at 10 mm from the centre of the blank by capacitive discharge, allowing the monitoring of the blank's temperature. For that purpose, the intensity of the applied current is controlled by a double current intensity/temperature regulation loop, allowing to follow the temperature set-point associated with the temperature measurement obtained from the thermocouple.

Due to the high temperatures aimed in the tests, the blank is formed by pressurized argon gas. The pressure is applied via a TESCOM ER5000 pressure controller. A pressure sensor (0 to 70 bar) located inside the cavity monitors the pressure. During the test, the deformation of the blank can be recorded by one of two kinds of non-contact measurement systems (see Fig. 3). The first one is a stereoscopic system (two CCD cameras, with GOM ARAMIS DIC system) to measure the surface of the dome apex (see Fig. 6). The second one is a laser

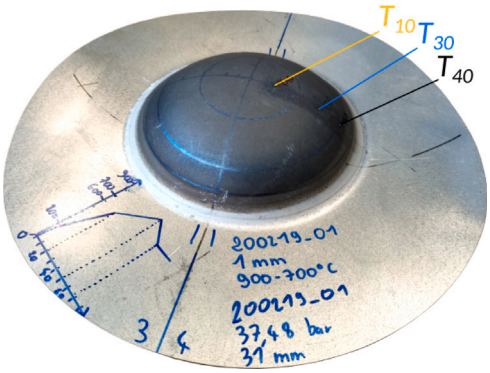

Fig. 7. Blank after preliminary test at 700 °C with indication of the position of the three thermocouples T_{10}, T_{30} and T_{40}.

profilometer (Keyence LJ-V7200). In this case, only a section passing through the centre of the top of the dome is measured. More details about this bulge-test device and its design can also be found in Demazel (2018).

3.3. Preliminary test analysis

In this section, the detailed analysis of a preliminary test of heating and bulging a boron blank, with the expansion device at 700 °C, is performed. The comparison between the experimental and numerical results of temperature evolution is also presented, in order to highlight the control parameters involved in the experimental setup. Fig. 7 shows the blank obtained at the end of the test.

To analyse the distribution and evolution of the temperature during the heating and expansion steps, three type *K* thermocouples were placed at 10, 30 and 40 mm from the centre, as shown in Fig. 7, and labelled T_{10}, T_{30} and T_{40}. The heat treatment imposed during this test, described by the T_{set} temperature, is composed of a heating step up to 900 °C in 50 s, a soaking during 10 s and a cooling to 700 °C, as presented in Fig. 8. The expansion step begins at 74 s.

Note that a study performed by ArcelorMittal (Demazel (2018) page 34) has shown that a heating time between 2 and 10 s, and a soaking time of at least 7 s lead to the target mechanical properties after quenching, which means that the austenization is completed and that the full martensitic structure is achieved after quenching. Maeno et al. (2020) shown also that, in case of hot bending of a 22MnB5 specimen heated by resistance heating, the microstructure is entirely martensitic after quenching for a soaking time between 5 and 10 s. Kolleck et al. (2009) shown that similar properties can be reached with induction heating in comparison to convective heating, for an uncoated 22MnB5 steel, with

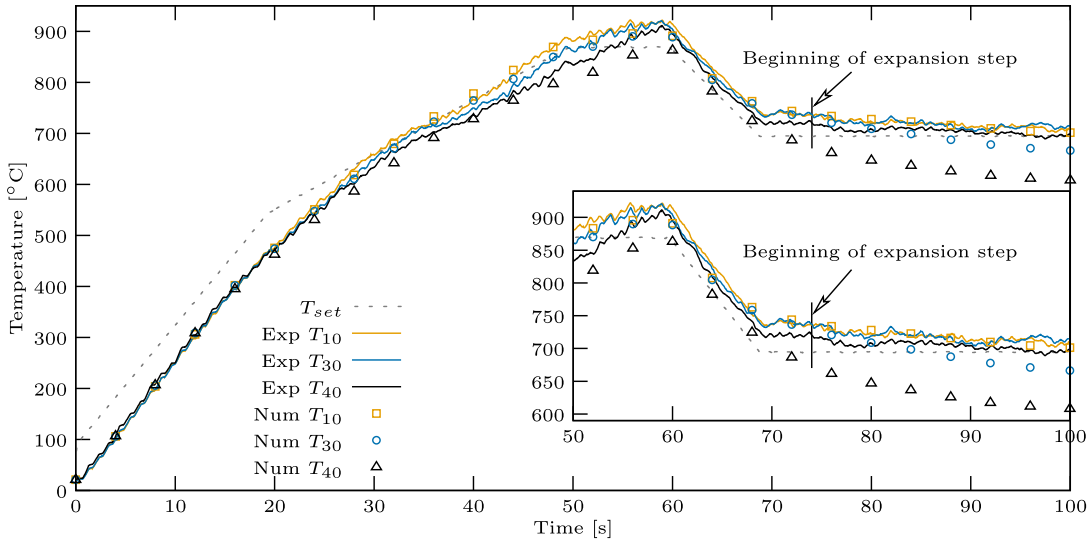

Fig. 8. Comparison between experimental and numerical results of temperature evolution for the three thermocouples during the heating, holding and expansion steps for the bulge test at 700 °C.

a much shorter heating time. In their case, due to the configuration of the induction-heating device, the shortest heating time guaranteeing austenitization was 35 s. Löbbe et al. (2016) also considered an uncoated 22MnB5 steel and an induction heating device to analyse the influence of the austenitization temperature (between 950 °C and 1100 °C) and dwell times (3 and 10 s) on the mechanical properties. The results show that a fully martensitic microstructure always develops. Moreover, it is consensual that the austenitization and homogenization process is strongly dependent on the microstructure constitution. In this context, Hou et al. (2021) analysed the effect of rapid heating on the microstructure and tensile properties of a novel uncoated, oxidation-resistant, press-hardening steel, comparing its properties to the ones obtained with a conventional coated 22MnB5 steel. The results show that a minimum soaking time of 120 s is required to achieve complete austenitization of the novel steel. Nevertheless, the steel under analysis presents no boron, which is the element that influences the hardenability the most, since it slows down the conversion into softer microstructures (Karbasian and Tekkaya, 2010).

During the test, the alternative current delivered by the electrical generator was managed by the PID controller to match the T_{set} temperature and the RMS current was recorded. The current profile delivered by the three pairs of electrodes is shown in Fig. 9a, while Fig. 9b presents the voltages measured under the pairs of electrodes. This allowed the comparison of the experimental temperature with the numerical results. For that, the current profile shown in Fig. 9a, was imposed in the numerical model. A constant application time, t_{app} of 0.7 s is used during this test. This means that the application time t_{app} had to be reduced when compared to the heating step of the numerical study presented in Section 3.3, in order to improve the temperature homogeneity and especially to avoid hot spots near the electrodes.

The heating step presents two different slopes in the temperature control loop, due to the constraints of the electrical generator used and the high influence of the integral term of the PID controller (see Fig. 8). The second slope is less steep than the first because the power of the generator is not sufficient to heat up as quickly, due to the endothermic reaction of the austenitization and the increase of thermal losses at high temperature. Therefore, the lower slope helps avoiding an increase of the integral term that leads to an overheating of the central area of the blank.

Fig. 7 shows that the blank presents a gradual change of colour from the centre to the outer edge. This evolution gives information on the thermal history of different positions of the blank and is indicative of an homogeneous temperature in its centre. Beyond the thermocouple T_{40} location, the colour of the blank changes, which corresponds to a high thermal gradient due to the cooling by the contact with the tools (see also Fig. 8).

Fig. 8 presents the comparison between the numerical and experimental temperature evolutions for the three thermocouples. The results show a good correlation during the heating step, with a maximum deviation of 30 °C at 60 s, for thermocouple T_{40}. After the cooling step, the gap between the measured and calculated temperatures for T_{40} gradually increase. This can be related with the fact that the simulation does not take into account the bulging deformation of the blank and, accordingly, the evolution of the geometry (especially the thickness decrease and the increase of the distance between electrodes passing through the blank centre, during the expansion step). However, the correlation between measured and calculated temperatures at the centre of the blank remains good.

This comparison shows that the numerical model results are consistent with the experimental ones. In essence, the model allowed the definition of the geometrical characteristics of the device, including size and position of the pairs of electrodes, as well as the global electrical parameters necessary for heating the sheet. It turns out to be particularly predictive: the parameters selected for the electrical and thermal contact resistances make it possible to obtain numerical results in agreement with the experimental ones. The advantage of the resistance heating method is also demonstrated, because the results show that this method allows to control the temperature of the blank also during the expansion step. Therefore, it is possible to reproduce almost all the steps of the hot stamping conditions: the heating and soaking times and the temperature during the expansion. The cooling rate to attain the temperature of the expansion step is not currently controlled. In the future, cooling devices could also be envisaged.

4. Experimental methods

In this section, the methods used to extract the stress–strain curves from the expansion tests, performed between 700 and 900 °C are presented. The experimental conditions used to perform tensile test on the Usibor®1500P steel, for the same range of temperature, in a Gleeble machine are also described.

4.1. Expansion tests

The stress–strain curve is evaluated applying the membrane theory that relates the stresses at the pole with the pressure, the radius of

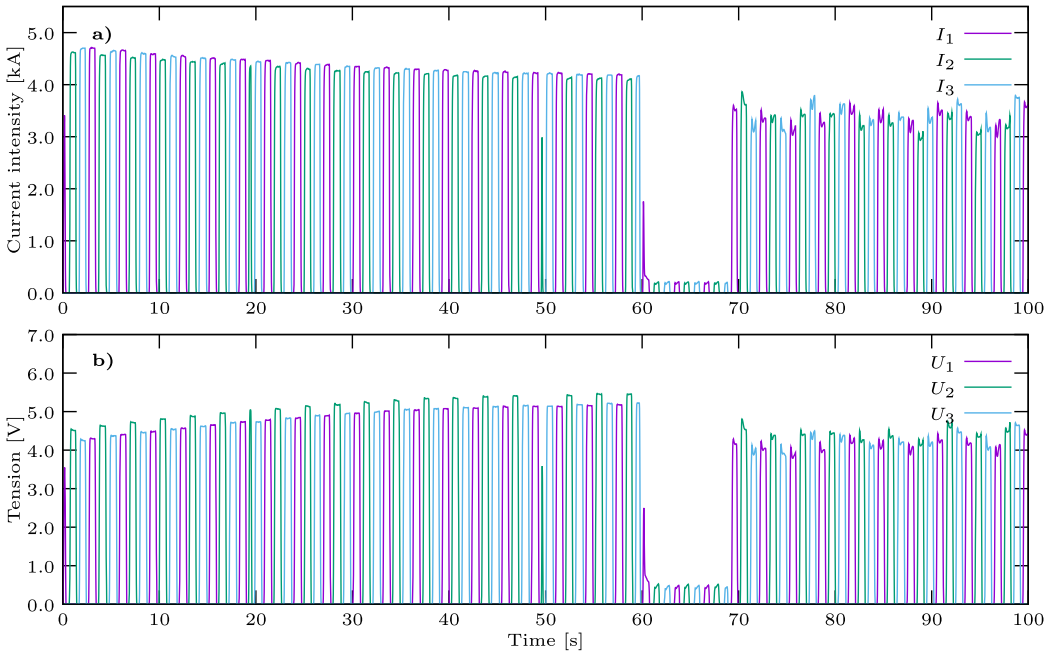

Fig. 9. Temporal evolution during the preliminary test of: (a) the experimental current in the three pairs of electrodes and imposed in the numerical simulation and (b) the voltages measured in the three pairs of electrodes.

curvature and the sheet thickness. There are mainly two possibilities as described, for example, in Boudeau et al. (2018). One follows a more simple experimental route, but requires the use of analytical models, which relate the evolution of the radius of curvature and the sheet thickness with the only variable measured: the pole height, h (see Fig. 3). The other one requires the acquisition of the geometry and strain distributions on the sheet surface during the bulge test, *i.e.* can only be applied using a DIC system. At high temperatures, DIC technique requires more experimental precautions, due to the difficulties associated with the calibration of the video system, taking into account the changes undergone by the surface of the blank with the increase of temperature and the large deformations (see Fig. 7).

In the following section, the main assumptions used to obtain the stress–strain curves from the bulge-test results are recalled. Then, the difficulties encountered when using a non-contact measurement system by DIC are described. Thus, an alternative is proposed, based on using a laser profilometer to measure the section of the dome during the expansion step. This requires the application of analytical methods to extract the stress–strain curve, which are also briefly recalled.

4.1.1. Evaluating the stress–strain curve using a DIC system

As the ratio between the initial thickness of the blank, which is either $t_0 = 0.9\,\text{mm}$ or $t_0 = 1\,\text{mm}$, and the die diameter $D = 120\,\text{mm}$ is lower than 1/33, as recommended by the (ISO16808, 2014) standard (see Fig. 4), the bending stress occurring during the bulge test can be neglected. Thus, the stress state at the centre of the sheet, assuming that the stress component normal to the sheet surface, σ_3, is equal to zero, can be obtained with the aid of the membrane theory:

$$\frac{\sigma_1}{\rho_1} + \frac{\sigma_2}{\rho_2} = \frac{p}{t} \tag{11}$$

where σ_1 and σ_2 are the principal stresses in the sheet surface, which are assumed to be coincident with the rolling and the transverse direction. ρ_1 and ρ_2 are the radii of curvature, at half thickness, in the same principal directions.

As mentioned in Chen et al. (2016), the stress state in the hydraulic bulge test can be considered in a first approximation as equibiaxial at the apex during deformation. For instance, the ISO 16808:2014 standard adopts the assumption that $\sigma_1 = \sigma_2 = \sigma_b$, where σ_b is the biaxial stress. This assumption, as explained by Reis et al. (2016), is valid for isotropic materials or orthotropic ones with similar properties for the rolling and transverse directions. In those cases, the radii of curvature also follow the assumption, such as $\rho_1 = \rho_2 = \rho$, which allow to simplify Eq. (11), such as:

$$\sigma_b = \frac{p\rho}{2t} \tag{12}$$

Although there is not a lot of information regarding the in-plane evolution of the Lankford coefficients of boron steels at high temperature, Merklein et al. (2007) showed that the austenitization reduces the grain orientation induced by the rolling process, leading to a planar anisotropy coefficient close to zero. Moreover, the flow stresses obtained from uniaxial tension tests performed at different orientations to the rolling direction present an fairly isotropic behaviour, as shown by Merklein and Lechler (2006). This allows adopting Eq. (12) to extract the stress–strain curves. The local thickness t of the blank's apex can be determined from the principal strains in the sheet plane, ε_1 and ε_2, at the same location, using the condition of volume consistency during plastic deformation:

$$\varepsilon_t = -(\varepsilon_1 + \varepsilon_2) \tag{13}$$

Knowing the thickness strain ε_t and the initial thickness of the blank, t_0, the thickness at the blank's apex can be estimated as follows:

$$t = t_0 \exp(-\varepsilon_t) \tag{14}$$

Note that the thermal expansion of the sheet in the bulge device causes the blank to expand, typically moving upwards, which maybe connected with the increase of the temperature of the air inside the cavity, causing its expansion. As the tests are performed under isothermal conditions, the thermal expansion can be assumed constant during the tests. Thus, the thermal expansion strain is calculated with the thickness strain at the instant the pressure start, $t_{i=P_{start}}$:

$$\varepsilon_{thermal} = \ln\left(\frac{t_{i=P_{start}}}{t_0}\right) \tag{15}$$

The current bulge strain ε_b is deducted from the total thickness strain as follows:

$$\varepsilon_b = -\ln\left(\frac{t}{t_0}\right) + \varepsilon_{thermal} \tag{16}$$

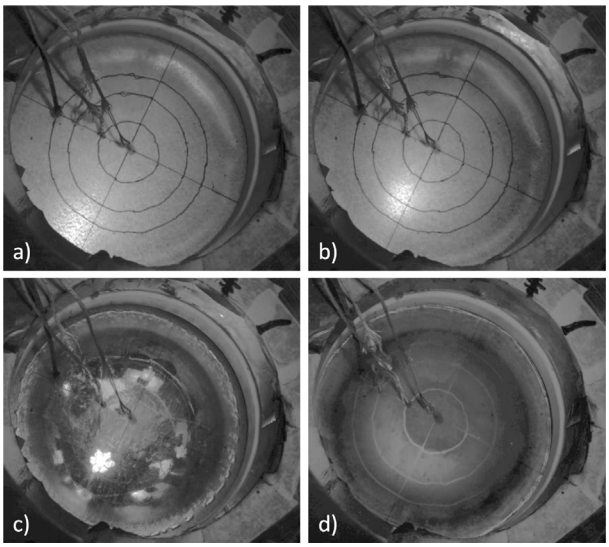

Fig. 10. Evolution of the Usibor®1500P blank with Al-Si coating during the heating step of a bulge test: (a) Initial conditions; (b) 400 °C; (c) 750 °C; (d) 900 °C.

This correction can overestimate the thermal strain since it also integrates some elastic component. Nevertheless, the correction of the elastic strain poses additional difficulties related with the knowledge of the evolution of the material elastic properties with the temperature. Therefore, it was decided to make no additional correction of the elastic component.

4.1.2. Difficulties of high temperature DIC

Outer surface 3D-DIC measurements are now classically used to monitor the surface geometry of the bulge dome during the expansion test, as used for example by Machado et al. (2012) for silicone elastomer and Lafilé et al. (2021) for small size bulge tests. The use of two CCD cameras enables the 3D-DIC system to capture the three-dimensional surface geometry and displacements of the visible surface of the blank, allowing the acquisition of the strain distributions on the sheet surface during the test. In this case, the 3D-DIC system is able to extract the major and minor strains, ε_1 and ε_2, as well as the radius of curvature ρ, *i.e.* the stress–strain curve can be directly evaluated. However, in high-temperature conditions, 3D-DIC systems can present some technical constrains, as explained by Aksenov and Sorgente (2020).

DIC systems require a calibration, partly dependent on the image luminosity and the reflective properties of the surface of the specimen. If an evolution of the surface properties of the specimen occurs during the test, the system can drift outside of its calibration window, leading to a monitoring failure during the test. The basic principle behind DIC methods is the application of a stochastic pattern or markings on the surface of the specimen which will be tracked. This pattern needs to withstand high temperature and large stretching without sliding off the blank's surface nor cracking.

Fig. 10 illustrates the surface evolution of a blank during the heating step of a high temperature bulge test, as seen by one of the cameras of the DIC setup, equipped with a blue filter. The DIC system used is a GOM ARAMIS 4M. The camera with a resolution of approximately $30\,\text{pixels}\,\text{mm}^{-2}$ recorded the motion of the specimen surface at the maximum frequency of 60 Hz. As explained in Section 2, the blank surface is coated with the Al-Si film, designed to alloy itself to the steel surface. The blank surface is clear and reflective in its as received state (Fig. 10a). The thermal expansion causes the blank to rise, this movement is observable by tracking the bright spot on the surface of the blank in Fig. 10b. However, as previously mentioned, during the melting of the coating, the blank surface appears as reflective as a mirror, as shown in Fig. 10c. In fact, the individual LEDs of the light used to illuminate the blank can be clearly distinguished for a brief moment once the blank reach 750 °C, as shown in Fig. 10c. After reaching the reflectiveness peak, the surface of the blank transitions to a dark and mat surface during the alloying of the coating to the steel. Fig. 10d shows this surface after the complete alloying of the Al-Si coating.

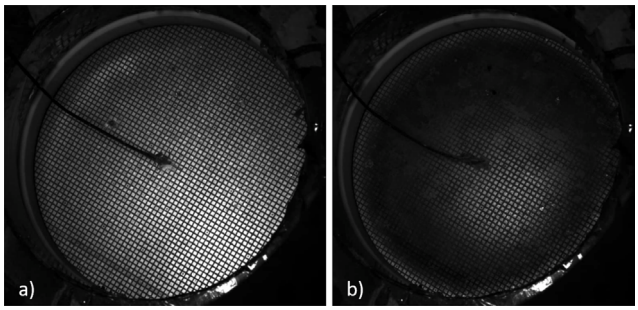

Fig. 11. Colour transition during a bulge test on a grided blank by electrolysis, as seen by the 3D-DIC camera system: (a) initial state; (b) state at 900 °C.

The colour transition observed is drastic enough to disturb any attempts to produce a conclusive and reliable DIC pattern for this high temperature range. In this context, Fig. 11 shows the colour transition observed in a blank with an etched grid by electrolysis, which was also tested ineffectively.

Unfortunately, all the tests performed with various high temperature paints were also unsuccessful. The severity of the colour evolution of the blank is such that the thickness of paint required to mask it is detrimental to the integrity of the paint. In fact, a too large thickness for the paint weakens its overall elasticity, producing cracks in the paint during the bulge expansion. These cracks are reduced or do not appear during tensile tests using the same paint. Moreover, the Al-Si coating layer deposited on the Usibor®1500P, shows some movement during the expansion test, due to the electrical current imposed during the heating (visible in Fig. 7). This can induce also movements of the paint pattern on the surface.

The nature of the bulge test setup forces the cameras to be on top of a cylindrical well (named tripod in Fig. 6) which constrains the position of the light source between the cameras of the DIC system. Due to the distance between the light source and the blank, it is difficult to focus the light only on the sample. Reflections from the walls of the cylindrical well towards the blank can lead to bright spots, as shown in Fig. 11-(a) in the top left region. The nature of the dome also promotes the creations of shadows, as the pole height increases with pressure. Moreover, the evolution of the contrast of the blank affects the capability of the cameras: the optimal exposure parameters for the beginning of the test are incompatible with the parameters required for the conditions at the end of the test. Ultimately, the light exposure of the blank and the relative limited dynamic range of the cameras, makes it difficult to optimize the lighting for the complete duration of the test. An alternative approach could be to perform the calibration at high temperature during the homogenization step, which in that case needs to be long enough in time.

4.1.3. Evaluating the stress–strain curve using a laser profilometer

To avoid all the technical challenges associated with DIC, a laser profilometer was selected as an alternative. Nevertheless, the profilometer can only monitor a line passing through the centre of the blank. Correspondingly, when using this type of device, it is necessary to use analytical formulas to estimate the evolution of the thickness and the radius of curvature, during the test (see Eq. (12)).

Several analytical models for the calculation of these variables have been proposed and tested for different experimental conditions and

materials. Lăzărescu et al. (2011) highlighted the very good agreement between the results obtained using DIC with the ones provided by analytical formula, for a DC04 steel. On the other hand, Boudeau et al. (2018) work emphasizes that, for anisotropic materials, DIC is required for post-processing experimental results of the bulge test. The radius of curvature ρ can be determined assuming that the blank as a spherical shape, dictated by the height of the pole's apex h and the die cavity radius r (see Fig. 1). In these conditions, as suggested in Hill (1950), the radius of curvature can be determined as:

$$\rho_{Hill} = \frac{r^2 + h^2}{2h} \tag{17}$$

However, Koç et al. (2011) demonstrated that the radius of curvature was consistently underestimated by Eq. (17) on bulge tests performed on AA5754 and AISI 201 materials, either at room temperature and at 150 °C. Panknin (1959) assumed that the blank's dome is also part of a sphere, but considered the influence of the fillet radius r_{die} of the die's cavity (see Fig. 1), defining the radius of curvature as:

$$\rho_{Panknin} = \frac{(r + r_{die})^2}{2h} + \frac{h}{2} - r_{die} \tag{18}$$

Eq. (18) leads to good agreements with experimental values for dome heights, normalized by the diameter of the cavity, of up to $h/r = 0.56$ (see further details in Gutscher et al. (2004)). The same observation was made by Liu et al. (2015) for an AA7075 at elevated temperatures. Therefore, Eq. (18) was the one adopted in this work and used to calculate the biaxial stress using Eq. (12).

Regarding analytical methods for the evaluation of the thickness evolution, Hill (1950) proposed the following relation:

$$t_{Hill} = t_0 \left(\frac{1}{1 + (h/r)^2} \right)^2 \tag{19}$$

Other authors, as Reis et al. (2016) have shown that the thickness evolution is also a function of other geometric parameters, as well as the work hardening coefficient and the orthotropic behaviour of the material. In this context, Min et al. (2017) proposed a method to calculate the effective stress at the specimen pole that takes into account the ratio of specimen thickness to the radius of curvature on the specimen outer surface, non-balanced biaxial curvatures in principal directions, the elastic deformation and bending effects.

Nevertheless, Eq. (19) is the one used in this work to evaluate the biaxial stress σ_b, with Eq. (12), and the bulge strain ε_b, with Eq. (16). Note that the height is the variable used to calculate the thickness and, consequently, to deduct the strain. Thus, the thermal strain is assumed to be the strain resulting from the height reached by the pole before the expansion starts (see Eq. (15)).

The laser profilometer is placed 240 mm above the blank (see Fig. 12), *i.e.* above the copper bars feeding the electrodes of the device shown in Fig. 6. A 3D printed adjustable mount assembly is used as shown in Fig. 12a. The line observed by the profilometer is aligned with the rolling direction of the blank, as shown in Fig. 12b. The length selected for the observed profile was 50 mm, centred around the centre of the blank, to ensure that the apex of the bulge is accurately captured. The profilometer has a functionality to calculate the radius of curvature directly but this option was not used since the method used by the KEYENCE controller is not available to the public. Eq. (18) was therefore preferred, since some examples available in the literature, such as Liu et al. (2015) indicate that it provides satisfactory results. Nevertheless, it should be mentioned that the differences observed between these two methods are negligible.

Before the test begins, *i.e.*, when the blank is at room temperature, clamped and flat, a reference profile is saved with the controlling software of the profilometer. From this reference profile, the height of the pole h is deducted by taking the shortest distance between the highest point of the current profile and the reference profile. The height of the pole is sampled at 50 Hz.

To validate the use of the laser profilometer, bulge tests were performed for an EN AW 6061-T6 aluminium alloy at 150 °C, which enables the application of both measurement systems. The stress–strain curves were obtained either with DIC or with the pole height evolution by the profilometer. The procedure used the equations previously presented, including the thermal strain correction. Comparison using the laser-profilometer of the stress–strain curves obtained by DIC and profilometer methods, presented in a previous work by Boyer et al. (2019), showed a good agreement. This validation enabled the application of the same method to analyse the expansion tests performed on boron steels, at high temperature.

4.2. Uniaxial tensile tests

Uniaxial tensile tests were performed with a Gleeble 3500 machine on Usibor®1500P steel. The specimen geometry is presented in Fig. 13a. The material used in these tests was sampled from a 0.9 mm thick sheet always with the length oriented along the rolling direction.

A type *K* thermocouple, with a diameter of 250 µm was welded on the centre of the specimen by capacitive discharge, to control the temperature during the test, as detailed in Fig. 13b. The strain measurements were performed in a 7 by 20 mm^2 zone in the centre of the sample using the DIC system, GOM ARAMIS 4M. The selected dimensions were slightly lower than the gauge area in order to minimize the influence of border effects and of the non-uniform distribution of the temperature field. Two video cameras with a resolution of approximately 30 pixels mm^{-2} recorded the motion of the specimen surface at the maximum frequency of 50 Hz. The cameras of the DIC system were placed above the specimen gauge area, while the thermocouple was welded on its backside surface, as shown in Fig. 13b. It should be mentioned that the calibration of the DIC system is easier for the tensile test than for the expansion tests, due to the smaller displacements that occur in the thickness direction, *i.e.* the distance between the specimen and the CCD cameras is kept constant.

4.3. Experimental conditions reproducing the quenching

Three temperatures of 900, 800 and 700 °C were chosen to reproduce the quenching conditions since they correspond to ones commonly used in the industry to perform forming operations. A schematic example of the temperature profile required to reproduce the quenching conditions at a prescribed temperature of 800 °C is presented in Fig. 14. Fig. 14a shows the conditions for the tensile test while Fig. 14b corresponds to the bulge test.

For both expansion and tensile loading conditions, after a first heating, an austenitization (soaking) step is imposed, followed by a cooling step to attain the prescribed temperature. The cooling is controlled in the Gleeble machine with compressed air jet, while it is provided by natural convection and the heat conduction to the tools in the bulge test. Subsequently, an homogenization step is performed to stabilized the temperature across the blank. After this homogenization step, the pressure is linearly increased in the cavity as shown in Fig. 14b for the bulge test, while the displacement of grips is linearly increased for the tension test (see Fig. 14a), leading to an initial strain rate of 0.02 s^{-1}. Table 2 presents the durations of the different steps as well as the cooling-rate used in the bulge and uniaxial tensile tests.

The main limitation of the bulge test device developed is that the tests cannot last longer than 120 s, to avoid the trigging of the thermal circuit break. The bulging time is therefore limited by the time left available after the heating, soaking, cooling and homogenization steps. Consequently, the two pressure rates selected were 0.06 and 0.12 MPa s^{-1}.

By comparing Figs. 14a and 14b, there are some differences in the thermal cycles adopted for the expansion and uniaxial tests, particularly, during the heating step. The heating time of the tensile tests is very high at the beginning to avoid the degradation of the DIC pattern

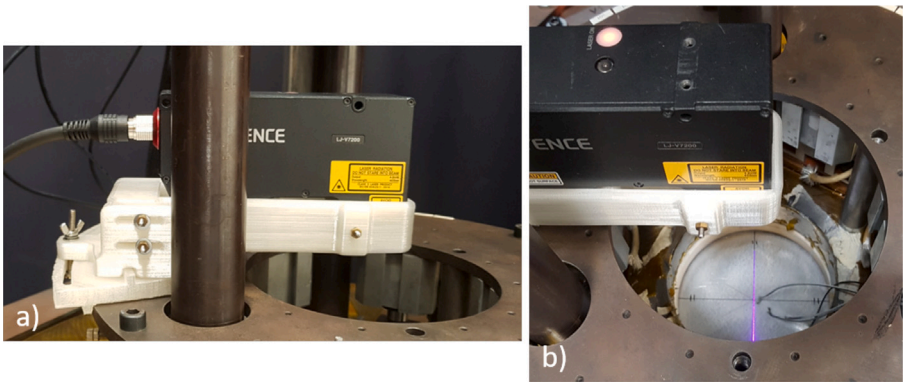

Fig. 12. Mounting of the profilometer in the expansion device: (a) Profile view of the 3D printed mount assembly; (b) View of the laser on the blank's surface.

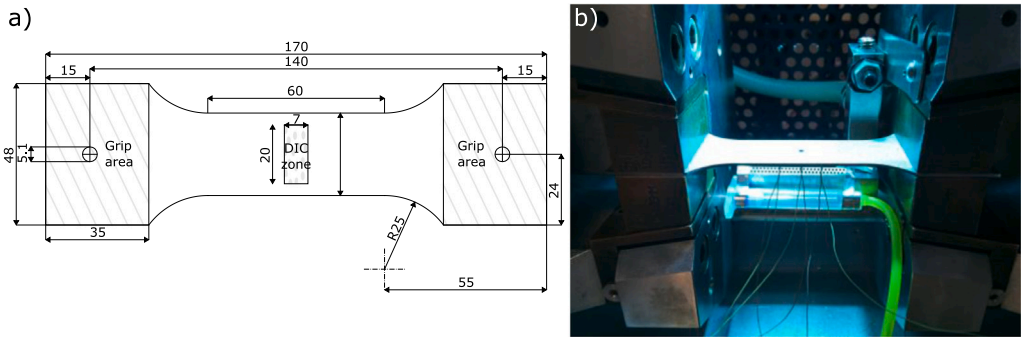

Fig. 13. Uniaxial tensile test: (a) Sample geometry; (b) Test sample in the Gleeble 3500 machine.

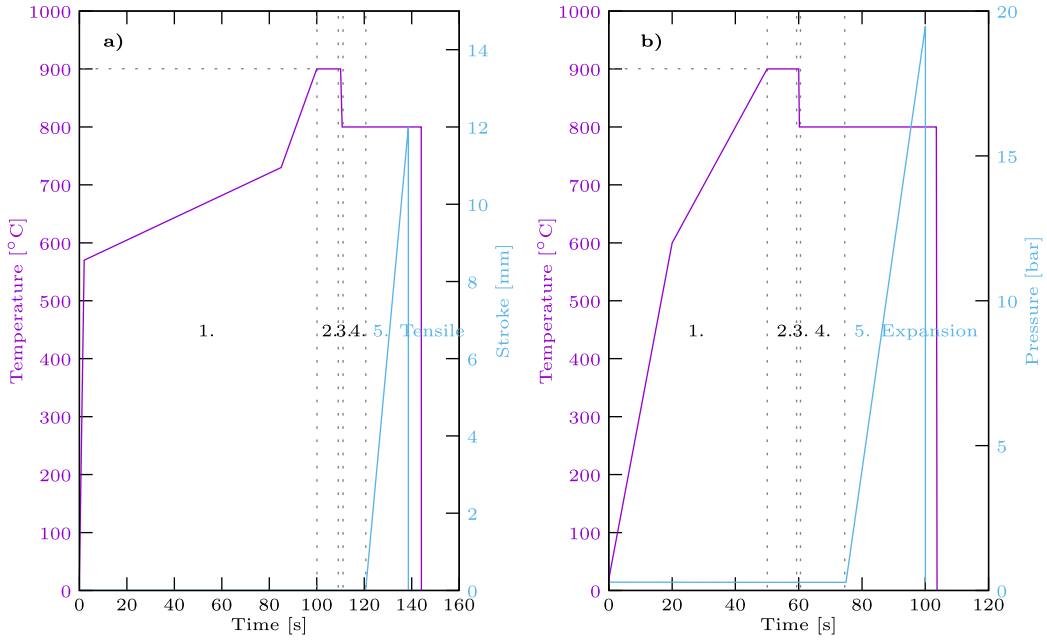

Fig. 14. Schematic illustrating of the temperature profile and the loading condition during (a) tensile and (b) bulge tests, to obtain the stress–strain curves at temperature at 800 °C. Numbers indicate the different steps: 1. Heating; 2. Soaking; 3. Cooling; 4. Homogenization and 5. Loading.

Table 2
Test cycle times for expansion and uniaxial tensile tests.

Conditions	1. Heating	2. Soaking	3. Cooling	4. Homogenization	5. Loading
Expansion	50 s	10 s	up to 12 s	5 to 10 s	up to 50 s
Tensile	100 s	10 s	up to 2 s	10 s	up to sample failure

by controlling the total time of the test. This alternative is adopted since the heating rate around the melting temperature of the coating is then drastically decrease to reduce the current and so the Lorentz forces which induce the coating displacement. This low heating rate avoids the displacement of the Al-Si coating during its melting and therefore the decorrelation of the blank's images during the calculation of the deformations with the DIC system. Finally, the heating rate between 730 to 900 °C is the same between tensile and bulge tests to obtain the same microstructure (e.g. grain size) between the two types of tests before the soaking step.

As mentioned in Section 3.3, a soaking time between 2 and 10 s is sufficient to form a fully martensitic structure. Therefore, a holding time of 10 s was selected to assure the full austenization of the specimen both for tensile and bulge tests.

As mentioned previously, the cooling rate in the bulge test is not controlled, contrary to the tensile test where compressed air jets can be used to quickly cool or quench. Thanks to these compressed air jets, the test temperature is attained faster and more precisely during tensile tests. For the bulge tests, the duration of the homogenization step varies between 5 to 10 s due to difficulties to control the temperature during the cooling.

Furthermore, the lowest the temperature of the test, the longer the blank will take to cool after the soaking period, limiting even more the bulging time left. As a result of this constraint, the pressure rate of 0.06 MPa s^{-1} is the slowest that can be applied while assuring that a reasonable strain value is attained, even for the lowest temperature studied of 700 °C. This is the reason why the maximum strain values reached in the bulge tests vary with the temperature and the pressure rate.

It is also important to mention that the control of the instant that the cooling step should end is more difficult for lower values of the prescribed temperature for the expansion tests. Note that the instructions for the control must be prepared before the start of the test. The temperature attained during the bulge step is conditioned by the PID and the error accumulated during the heating step is compensated on the bulging step by the Integral term of the PID (see also Fig. 8). This compensation mechanism of the PID regulation contributes to the difficulties encountered in tests reproducibility. Four tests were successfully performed with a pressure rate of 0.12 MPa s^{-1}, for each temperature. For the 0.06 MPa s^{-1} pressure rate, only two tests were performed for the 900 and 800 °C temperature, while only one test was successfully performed at 700 °C. The test that shows a better evolution of the prescribed temperature and pressure rate, for each condition, is defined as the most representative for each test conditions and is the one presented in this work.

This also explains why the expansion tests analysed in this study correspond to blanks with different initial thickness, as presented in Table 3. The first batch received presented a thickness of 0.9 mm while later batches with 1.0 mm were supplied. For 900 °C, the tests were performed with a thickness of 0.9 mm. The tests at 800 °C correspond to a thickness of 1.0 mm. For 700 °C, the tests reported with the two pressure rates were performed with different thicknesses. Only the blanks tested at 900 °C and the blank tested at 800 °C with 0.12 MPa s^{-1} pressure rate reached the bursting pressure. For the other temperatures and pressure rates, this is not achieved due to the limitation imposed by the total time for the test. Table 3 summarizes the initial blank thickness and if bursting was reached for each test performed.

The uniaxial tensile tests were carried out using displacement control, with a prescribed cross-head velocity to obtain the initial strain rate of 0.02 s^{-1}. Nevertheless, under these conditions, the strain rate can vary during the test, since the length of the specimen is continuously increasing. On the other hand, in the expansion tests, it is known that a constant pressure rate does not lead to a constant strain rate.

The strain rate in each test was calculated by dividing the increment of strain per the increment of time, using all consecutive data points available. Nevertheless, it is known that the use of this forward difference to evaluate the strain rate leads to some noise. This is particularly critical for the expansion test, because the bulge strain is derived from the height of the dome of the blank. The dome height measurement can be affected by the profilometer sensor accuracy, which can result in oscillations on the height. These oscillations can pollute the strain rate calculation and its subsequent visualization. Smoothing techniques can be applied to prevent the apparition of this phenomenon. In this study, for bulge test results, a sampling filter was applied, considering one out of four data point available.

Table 3
Bulge test blank initial thickness and bursting conditions at the end of the test for 700, 800 and 900 °C for 0.06 and 0.12 MPa s^{-1} pressure rates.

Test temperature (°C)	Parameters	0.06 MPa s^{-1}	0.12 MPa s^{-1}
900	t_0 (mm)	0.9	0.9
	Burst	Yes	Yes
800	t_0 (mm)	1.0	1.0
	Burst	No	Yes
700	t_0 (mm)	1.0	0.9
	Burst	No	No

5. Results and discussion

The biaxial stress–strain curves for both pressure rates and three temperatures are presented in Fig. 15a. This figure presents also the stress–strain curves for the uniaxial tensile tests for the three temperatures performed with an initial strain rate of 0.02 s^{-1}

These evolutions are shown in function of the bulge stress and strain for the expansion test and of the true stress and strain for tensile test. Note that the direct comparison is possible when assuming that the material shows an isotropic behaviour (see discussion in Section 4.1.1). Dashed lines with crosses are used to represent tensile tests whereas the continuous lines concerns bulge tests results obtained with a pressure rate of 0.06 MPa s^{-1} and the ones for 0.12 MPa s^{-1} are represented with dashed lines.

Concerning tensile tests, although three tests were conducted for each set of conditions, since the results show high reproducibility, only one was selected to be presented in this figure. Moreover, the results are plotted only up to the instant the maximal force is attained. Due to this condition, it should be mentioned that the maximal strain range observed is within 0.10 at 900 °C, 0.17 at 800 °C and 0.096 at 700 °C. Globally, the uniaxial tensile tests show that the increase of temperature leads to an overall decrease of the stress.

As previously mentioned, the difficulty to obtain a successful expansion test with the lowest temperature and the 0.06 MPa s^{-1} pressure rate is high. However, it should be mentioned that the bulge stress–strain results for the 0.12 MPa s^{-1} pressure rate show high reproducibility. Moreover, the evolution of the prescribed temperature and the pressure rate of the single test performed at 0.06 MPa s^{-1} and 700 °C, gives confidence that it is representative of the material's behaviour for those conditions.

The evolution of the strain rate during the expansion tests is presented in Fig. 15b. This figure presents also the strain rate evolution during the tensile test performed at a strain rate of 0.02 s^{-1}. The strain rate is almost constant for all the tensile tests, showing a slight increase at the end of the test. Unlike tensile tests, the strain rate during the expansion tests presents an increasing trend from the beginning. The linear increase of the pressure in the cavity leads to a continuous increase of the strain rate over the tests, regardless of the temperature or pressure rate. The strain rate at the beginning of the test is 0.001 s^{-1} and afterwards increases fast, until reaching a strain rate from which it starts to increase more slowly until the end of the tests. These results show that the only strain rate for which it is reasonable to make

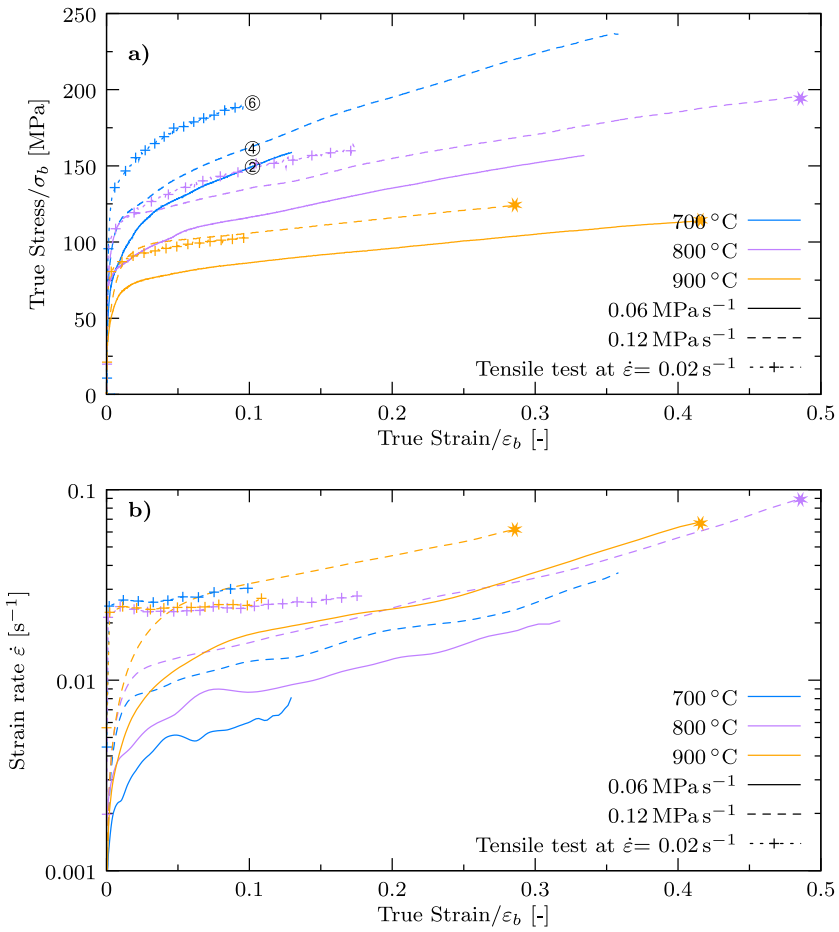

Fig. 15. Expansion results at 700, 800 and 900 °C for 0.06 and 0.12 MPa s^{-1} pressure rates and comparison with uniaxial tensile tests for an initial strain rate of 0.02 s^{-1}; (a) True Stress or σ_b *versus* True Strain or ε_b; (b) Strain rate *versus* True strain or ε_b. (✶ indicates the burst of the specimen, the number indicates the instant the strain value of 0.096 is attained for ② 0.06 MPa s^{-1}, ④ 0.12 MPa s^{-1} and ⑥ for tensile test, all performed at 700 °C).

comparisons between both type of tests is the lowest one used in the tensile test, *i.e.* 0.02 s^{-1}.

Only at 900 °C the expansion tests were performed until burst. In this case, the test at 0.12 MPa s^{-1} reaches a maximum strain value lower than the one of the tests performed at 0.06 MPa s^{-1}, and both have deformations larger than for tensile tests. The other tests were not performed up to the blank failure, preventing any further discussion about the influence of the strain rate on the formability.

Globally, the results from the expansion tests lead to conclusions similar to the ones from tensile tests, in terms of thermal dependence. The hardening evolution of the two expansion tests performed at the same temperature are similar, with identical differences between the curves for the two pressure rates, which indicate a positive strain rate sensitivity. However, Fig. 15a shows that the evolution of the hardening slope of the expansion tests presents non-negligible differences from the one obtained from uniaxial tensile results.

At 900 °C, the yield strength is comparable between the expansion at 0.12 MPa s^{-1} and the tensile test. The tensile test stress is quite similar to the one obtained with the higher pressure rate. Moreover, the expansion test keeps a constant hardening slope although the strain rate keep increasing. The relatively constant strain rate value of the tensile test is globally higher than the one of the biaxial, which may explain the slightly higher initial yield stress value attained for the tensile test.

At 800 °C, the yield strength of the tensile test is higher than the ones of the expansion tests. For this temperature, the relatively constant strain rate value of the tensile tests is globally higher than the one of the biaxial, which may explain the slight higher stress value attained for the tensile test.

At 700 °C, the yield tensile stress is also higher than the one observed for both expansion test. As for the other temperatures, this can be related with the higher strain rate value attained in the tensile test, when compared with the bulge tests. In fact, Fig. 15b shows that the differences in the strain rate values between both type of tests are higher at lower temperatures. The expansion tests performed at 0.12 MPa s^{-1} and 0.06 MPa s^{-1} show a similar hardening trend, with a constant gap in the stress value, which seems to correlate well with the difference in strain rate. Thus, although blank's with different initial thickness were used that does not seem to affect the hardening behaviour. Note that this direct comparison is possible when assuming that the material shows an isotropic behaviour (see discussion in Section 4.1.1) and that the austenization step reduces the differences in the hardening behaviour of rolled sheets with different thickness. It is also possible to note that the strain rate evolution in expansion follows a linearly increasing trend, except the test at 700 °C and 0.06 MPa s^{-1}, which never reaches the steady increasing trend.

Although the main differences observed on the stress–strain curves between tensile and bulge tests at 700 °C can be explained based on the different strain rate values, it is interesting to analyse the influence of the cooling rate in the metallurgical transformations of the 22MnB5 steel. Fig. 16 presents the Continuous Cooling Transformation (CCT) diagram of undeformed Usibor®1500P presented in Ravier et al. (2003). This CCT diagram shows the different phase transformations that can occur depending on the cooling rate. Despite the durations of each step (heating, soaking and cooling) are different from those of the tests performed in this study, it allows to visualize the phase transformations that may occur during the uniaxial tension and bulging tests.

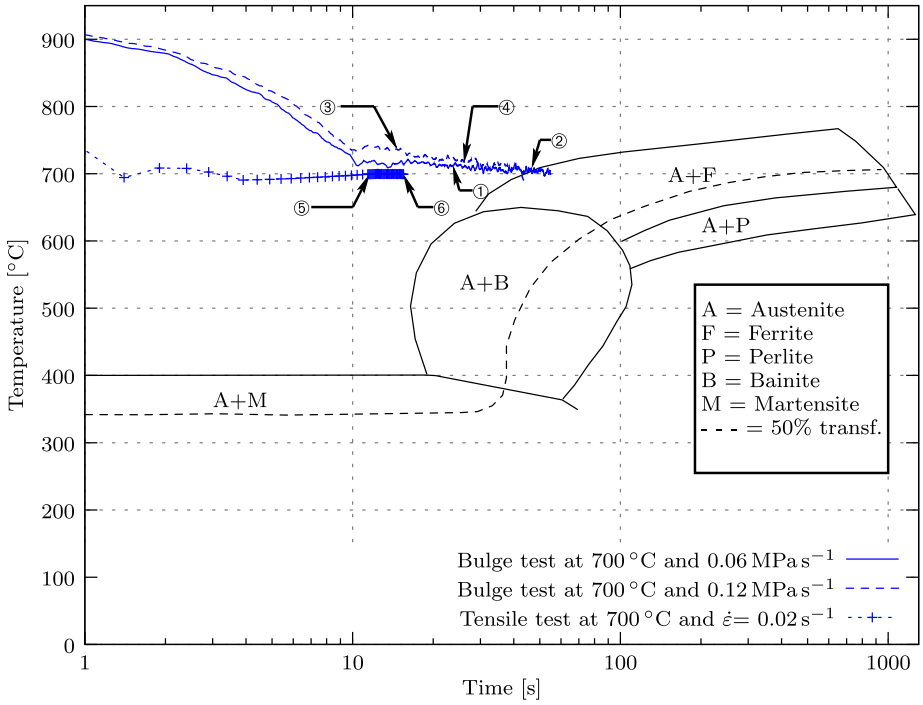

Fig. 16. Continuous Cooling Transformation diagram from Ravier et al. (2003) with the evolution of the temperature *versus* time for the bulge test at 700 °C for 0.06 and 0.12 MPa s^{-1} pressure rates and uniaxial tensile test with an initial strain rate value of 0.02 s^{-1} (the odd numbers indicate the start of the forming stage: ① 0.06 MPa s^{-1}, ③ 0.12 MPa s^{-1} and ⑤ for tensile test; the even numbers indicate the instant the strain value of 0.096 is attained for: ② 0.06 MPa s^{-1}, ④ 0.12 MPa s^{-1} and ⑥ for tensile test).

It is also important to notice that during the cooling phase, the deformation of austenite has an influence on the transformation kinetics. Fan et al. (2007) showed that this deformation of austenite may increase the ferrite nucleation rate. In fact, a change in the austenitic content of the sample affects the stress–strain response during the forming. Moreover, the prestrain is also known to promote metallurgical transformations, as shown in Reitz et al. (2022), with the shift of the A+F and A+B regions of the CCT diagram to the left.

In Fig. 16, the temperature evolution in function of time for the two bulge tests performed at 700 °C are compared with the one of tensile test performed at 700 °C, with an initial strain rate value of 0.02 s^{-1}. As shown in Table 2, bulge and tensile tests were performed with different cooling rates, which are also evident in Fig. 16. Although the CCT diagram was obtained for a different soaking time and cooling rate, it is possible to observe that the higher cooling rate used in the uniaxial tensile tests is better suited to ensure the material microstructure is fully austenitic, at the end of the test, even when applying a smaller strain rate (tests with longer duration). According to Fig. 16, the smaller cooling rate attained with the bulge test device can promote the formation of ferrite in the microstructure. This may also contribute to some differences in the hardening behaviour between tensile and expansion tests at 700 °C. A better control of the cooling performance of the expansion device would allow a better prediction of the time required to reach the test temperature. Thus, it would allow to trigger the expansion phase sooner, reducing the possibility of microstructural changes in the blank during the expansion phase.

6. Conclusion

This work addresses one of the major challenges in the acquisition of the biaxial stress–strain curve from the hydraulic bulge test at high temperature: ensuring a homogeneous temperature field on the dome area. To overcome this problem, an innovative procedure, based on the heating Joule effect, was designed with the aid of a multi-physic model using COMSOL Multiphysics®. This heating method was selected since the aim is to uniformly heat and austenize complex shape blanks of Usibor®1500P steel in conditions that resemble the ones used on hot forming processes (i.e. considering short heating and soaking times for an austenitization temperature of 900 °C). The heating method developed allows not only imposing a uniform temperature in the dome area, but also maintaining it during the bulging.

A new hydraulic bulge test device at high temperature was implemented showing good correlation with the numerical model and demonstrating its capability to reproduce accurately the temperature cycle of hot forming. Nevertheless, the short time to calibrate the DIC system at high temperature, combined with the degradation of the pattern (amplified by the biaxial deformation) and by the presence of the Al-Si coating, resulted in the inability to apply DIC techniques to measure the principle strains during the process and, consequently, the curvature and the thickness evolutions. These difficulties are carefully detailed since this is other of the major challenges in the acquisition of the biaxial stress–strain curve from the hydraulic bulge test at high temperature. To circumvent this limitation, a compromise alternative was adopted that uses a laser profilometer. This means that the curvature and thickness are determined using analytical expressions that relate their evolutions with the pole height.

The mechanical behaviour of the Usibor®1500P steel was also evaluated in uniaxial tensile conditions on a Gleeble machine with a DIC system and the results were compared with the ones obtained using the new expansion device for three different temperatures. Uniaxial tensile tests were performed for a single strain rate value while two pressure rate values were selected for the bulge tests. The constant pressure rate of the bulge test resulted in a continuous increase of the strain rate during the tests. The uniaxial tensile tests show that the increase of temperature leads to an overall decrease of the stress. The bulge test results also capture the decrease of stress with temperature and highlight the positive strain rate sensitivity.

Nevertheless, the constant pressure rate applied during the bulge test results in a continuous increase of the strain rate during the tests. The control of the strain-rate is very difficult because it requires the acquisition of the thickness strain, continuously during the test. This is another major challenge in the acquisition of the biaxial stress–strain

curve from the hydraulic bulge test at high temperature, which was not tackled in this work. Despite the difficulties reported in this study for the Usibor®1500P steel, the new hydraulic bulge test device enables a fast heating of the specimens to hot temperature conditions, assuring a homogeneous temperature field in the dome while enabling the acquisition of the principle strains through DIC, as previously reported for an aluminium alloy by Boyer et al. (2019).

CRediT authorship contribution statement

A. Boyer: Investigation, Validation, Formal analysis, Writing – original draft. **N. Demazel:** Investigation, Conceptualization, Methodology, Software, Writing – review & editing. **J. Coër:** Conceptualization, Investigation, Methodology. **M. Carin:** Conceptualization, Software, Writing – review & editing, Supervision, Project administration. **H. Laurent:** Conceptualization, Methodology, Writing – review & editing, Visualization, Supervision, Funding acquisition, Project administration. **M.C. Oliveira:** Data curation, Resources, Writing – review & editing, Supervision, Funding acquisition, Project administration.

Declaration of competing interest

The authors declare that they have no known competing financial interests or personal relationships that could have appeared to influence the work reported in this paper.

Data availability

Data will be made available on request.

Acknowledgements

This work was part of the ANR PRICECAT project, which is supported by the National Agency of Research (ANR) under the ANR-13-RMNP-0009-03. This research was also supported by the French Ministry of Higher Education and the Portuguese Foundation for Science and Technology (FCT) via the projects PTDC/EME-EME/30592/2017 (POCI-01-0145-FEDER-030592), PTDC/EME-APL/29713/2017 (POCI-01-0145-FEDER-029713), UIDB/00285/2020 and LA/P/0112/2020. The authors would like to thank the society SREM Technologies-France (http://www.srem.fr/fr/), for the design and conception of the device and for the furniture of the electrical generator. They also gratefully acknowledge research support from R. Canivenc, J. Favero, H. Salmon-Legagneur and G. Brun from ArcelorMittal (Montataire-France) and the technical support provided by A. Jegat (IRDL) during the experimental campaigns.

References

Abu-Farha, F., Hector, L.G., 2011. Sheet orientation effects on the hot formability limits of lightweight alloys. J. Manuf. Sci. Eng. 133 (6), 061005. http://dx.doi.org/10.1115/1.4004850.

Aksenov, S., Sorgente, D., 2020. Determination of biaxial stress–strain curves for superplastic materials by means of bulge forming tests at constant stress. CIRP J. Manuf. Sci. Technol. 31, 618–627. http://dx.doi.org/10.1016/j.cirpj.2020.09.002.

Alharthi, H., Hazra, S., Alghamdi, A., Banabic, D., Dashwood, R., 2018. Determination of the yield loci of four sheet materials (AA6111-T4, AC600, DX54D+Z, and H220BD+Z) by using uniaxial tensile and hydraulic bulge tests. Int. J. Adv. Manuf. Technol. http://dx.doi.org/10.1007/s00170-018-2339-5.

Ayres, R.A., Wenner, M.L., 1979. Strain and strain-rate hardening effects in punch stretching of 5182-0 aluminum at elevated temperatures. MTA 10 (1), 41–46. http://dx.doi.org/10.1007/BF02686404.

Banabic, D., Vulcan, M., Siegert, K., 2005. Bulge testing under constant and variable strain rates of superplastic aluminium alloys. CIRP Ann. 54 (1), 205–208. http://dx.doi.org/10.1016/S0007-8506(07)60084-5.

Bariani, P.F., Bruschi, S., Ghiotti, A., Turetta, A., 2008. Testing formability in the hot stamping of HSS. CIRP Ann. - Manuf. Technol. 57 (1), 265–268. http://dx.doi.org/10.1016/j.cirp.2008.03.049.

Behrens, B., Hübner, S., Schrodter, J., Uhe, J., 2015. Conductive heating opens up various new opportunities in hot stamping. In: Proceedings of 5Th International Conference on Accuracy in Forming. Toronto, pp. 157–173.

Blaise, A., Bourouga, B., Abdulhay, B., Dessain, C., 2013. Thermal contact resistance estimation and metallurgical transformation identification during the hot stamping. Appl. Therm. Eng. 61 (2), 141–148. http://dx.doi.org/10.1016/j.applthermaleng.2013.07.041.

Bleck, W., Blumbach, M., 2005. Laser-aided flow curve determination in hydraulic bulging. Steel Res. Int. 76 (2–3), 125–130. http://dx.doi.org/10.1002/srin.200505983.

Boudeau, N., Vitu, L., Laforge, N., Malécot, P., Michel, G., Milesi, M., Manov, S., 2018. How to post-process experimental results from the Flange bulging test? Application to the characterization of a Zinc alloy. IOP Conf. Ser.: Mater. Sci. Engi. 418, 012086. http://dx.doi.org/10.1088/1757-899X/418/1/012086.

Boyer, A., Laurent, H., Oliveira, M.C., 2019. Evaluation of the stress vs strain curve using a high temperature bulge test device. IOP Conf. Ser.: Mater. Sci. Eng. 651, 012048. http://dx.doi.org/10.1088/1757-899X/651/1/012048.

Braun, A., Bambach, M., Hirt, G., 2014a. Investigation of a bulge test at high temperatures and high strain rates using a finite-element simulation study. Key Eng. Mater. 622–623, 300–307. http://dx.doi.org/10.4028/www.scientific.net/KEM.622-623.300.

Braun, A., Storz, J., Bambach, M., Hirt, G., 2014b. Development of a pneumatic bulge test for high temperatures and controlled strain rates. Adv. Mater. Res. 1018, 245–252. http://dx.doi.org/10.4028/www.scientific.net/AMR.1018.245.

Braun, A., Waerder, M., Hirt, G., 2016. Forming limit and Flow curve determination of hot stamping steels using a hot-gas-bulge-test. In: Forming Technology Forum 2016. Munich.

Chen, K., Scales, M., Kyriakides, S., Corona, E., 2016. Effects of anisotropy on material hardening and burst in the bulge test. Int. J. Solids Struct. 82, 70–84. http://dx.doi.org/10.1016/j.ijsolstr.2015.12.012.

Demazel, N., 2018. Développement d'une solution de chauffage par conduction électrique pour l'emboutissage des aciers trempants : approche numérique et expérimentale (Ph.D. thesis). Université Bretagne Sud, URL http://www.theses.fr/s131042.

Demazel, N., Carin, M., Laurent, H., Le Masson, P.L., Coër, J., Favero, J., Canivenc, R., Glock, F., Graveleau, S., 2016. Numerical optimization of Joule heating process of Usibor® 1500 automotive blanks. In: NUMIFORM 2016. p. 3, URL http://numiform2016.utt.fr/Papers/91.pdf.

Demazel, N., Laurent, H., Carin, M., Le Masson, P., Salmon-Legagneur, H., 2021. A direct resistance heating method for shaped blank. J. Manuf. Process. 62, 772–783. http://dx.doi.org/10.1016/j.jmapro.2020.12.056.

Demazel, N., Laurent, H., Coër, J., Carin, M., Masson, P.L., Favero, J., Canivenc, R., Salmon-Legagneur, H., 2018. Investigation of the progressive hot die stamping of a complex boron steel part using numerical simulations and Gleeble tests. Int. J. Adv. Manuf. Technol. 1–15. http://dx.doi.org/10.1007/s00170-018-2532-6.

Deng, T., Li, D., Li, X., 2018. Temperature variation model of titanium alloy L-angle profile in hot stretch forming with resistance heating. Int. J. Adv. Manuf. Technol. 95 (5–8), 2105–2110. http://dx.doi.org/10.1007/s00170-017-1334-6.

Dutta, A., Mukherjee, A.K., 1992. Superplastic forming: an analytical approach. Mater. Sci. Eng. A 157 (1), 9–13. http://dx.doi.org/10.1016/0921-5093(92)90092-F.

Fan, D., Kim, H., Birosca, S., De Cooman, B.C., 2007. Critical review of hot stamping technology for automotive steels. In: Proceedings from the Materials Science & Technology Conference MS&T 2007. 1, Detroit, Michigan, USA, pp. 98–109.

Groche, P., Huber, R., Dörr, J., Schmoeckel, D., 2002. Hydromechanical deep-drawing of aluminium-alloys at elevated temperatures. CIRP Ann. - Manuf. Technol. 51 (1), 215–218. http://dx.doi.org/10.1016/S0007-8506(07)61502-9.

Gutscher, G., Wu, H.-C., Ngaile, G., Altan, T., 2004. Determination of flow stress for sheet metal forming using the viscous pressure bulge (VPB) test. J. Mater Process. Technol. 146 (1), 1–7. http://dx.doi.org/10.1016/S0924-0136(03)00838-0.

Hill, R., 1950. A theory of the plastic bulging of a metal diaphragm by lateral pressure. Philos. Mag. J. Sci. 41 (322), 1133–1142. http://dx.doi.org/10.1080/14786445008561154.

Hou, Z., Min, J., Wang, J., Lu, Q., He, Z., Chai, Z., Xu, W., 2021. Effect of rapid heating on microstructure and tensile properties of a novel coating-free oxidation-resistant press-hardening steel. JOM 73 (11), 3195–3203. http://dx.doi.org/10.1007/s11837-021-04877-7.

ISO16808, 2014. Metallic materials – Sheet and strip – Determination of biaxial stress-strain curve by means of bulge test with optical measuring systems. URL https://www.iso.org/standard/57777.html.

Jocham, D., Norz, R., Volk, W., 2017. Strain rate sensitivity of DC06 for high strains under biaxial stress in hydraulic bulge test and under uniaxial stress in tensile test. Int. J. Mater. Form. 10 (3), 453–461. http://dx.doi.org/10.1007/s12289-016-1293-8.

Jovane, F., 1968. An approximate analysis of the superplastic forming of a thin circular diaphragm: Theory and experiments. Int. J. Mech. Sci. 10 (5), 403–427. http://dx.doi.org/10.1016/0020-7403(68)90005-2.

Karbasian, H., Tekkaya, A., 2010. A review on hot stamping. J. Mater Process. Technol. 210 (15), 2103–2118. http://dx.doi.org/10.1016/j.jmatprotec.2010.07.019.

Kaya, S., Altan, T., Groche, P., Klöpsch, C., 2008. Determination of the flow stress of magnesium AZ31-O sheet at elevated temperatures using the hydraulic bulge test. Int. J. Mach. Tools Manuf. 48 (5), 550–557. http://dx.doi.org/10.1016/j.ijmachtools.2007.06.011.

Koç, M., Billur, E., Cora, Ö.N., 2011. An experimental study on the comparative assessment of hydraulic bulge test analysis methods. Mater. Des. 32 (1), 272–281. http://dx.doi.org/10.1016/j.matdes.2010.05.057.

Kolleck, R., Veit, R., Hofmann, H., Lenze, F., 2008. Alternative heating concepts for hot sheet metal forming. In: 1st International Conference on Hot Sheet Metal Forming of High-Performance Steel. pp. 239–246.

Kolleck, R., Veit, R., Merklein, M., Lechler, J., Geiger, M., 2009. Investigation on induction heating for hot stamping of boron alloyed steels. CIRP Ann. 58 (1), 275–278. http://dx.doi.org/10.1016/j.cirp.2009.03.090.

Lafilé, V., Galpin, B., Mahéo, L., Roth, C.C., Grolleau, V., 2021. Toward the use of small size bulge tests: Numerical and experimental study at small bulge diameter to sheet thickness ratios. J. Mater Process. Technol. 291, 117019. http://dx.doi.org/10.1016/j.jmatprotec.2020.117019.

Lee, J.-Y., Xu, L., Barlat, F., Wagoner, R.H., Lee, M.-G., 2013. Balanced biaxial testing of advanced high strength steels in warm conditions. Exp. Mech. 53 (9), 1681–1692. http://dx.doi.org/10.1007/s11340-013-9758-x.

Li, D., Ghosh, A.K., 2004. Biaxial warm forming behavior of aluminum sheet alloys. J. Mater Process. Technol. 145 (2), 281–293. http://dx.doi.org/10.1016/j.jmatprotec.2003.07.003.

Li, C., Jiang, S., Zhang, K., 2012. Pulse current-assisted hot-forming of light metal alloy. Int. J. Adv. Manuf. Technol. 63 (9–12), 931–938. http://dx.doi.org/10.1007/s00170-012-3934-5.

Li, Y., Li, S., Chen, Y., Han, G., 2019. Constitutive parameters identification based on DIC assisted thermo-mechanical tensile test for hot stamping of boron steel. J. Mater Process. Technol. 271, 429–443. http://dx.doi.org/10.1016/j.jmatprotec.2019.04.020.

Liang, W.K., Wang, L., Liu, Y., Wang, Y.L., Zhang, Y.S., 2014. Blank shape sensitivity on temperature distribution of hot stamping boron steel through conduction heating. Adv. Mater. Res. 1063, 211–214. http://dx.doi.org/10.4028/www.scientific.net/AMR.1063.211.

Liang, W., Wang, H., Wang, Q., Liu, Q., Zhang, Y., 2021. Application of conduction heating on hot stamping of front bumper. Int. J. Adv. Manuf. Technol. 112 (11), 3177–3188. http://dx.doi.org/10.1007/s00170-021-06618-1.

Liu, K., Lang, L., Cai, G., Yang, X., Guo, C., Liu, B., 2015. A novel approach to determine plastic hardening curves of AA7075 sheet utilizing hydraulic bulging test at elevated temperature. Int. J. Mech. Sci. 100, 328–338. http://dx.doi.org/10.1016/j.ijmecsci.2015.07.002.

Löbbe, C., Hering, O., Hiegemann, L., Tekkaya, A.E., 2016. Setting mechanical properties of high strength steels for rapid hot forming processes. Materials 9 (4), http://dx.doi.org/10.3390/ma9040229.

Loulou, T., Masson, P.L., Rogeon, P., 2006. Thermal characterization of resistance spot welding. Numer. Heat Transfer B 49 (6), 559–584. http://dx.doi.org/10.1080/10407790500433986, arXiv:http://dx.doi.org/10.1080/10407790500433986.

Lăzărescu, L., Comşa, D.S., Banabic, D., 2011. Determination of stress-strain curves of sheet metals by hydraulic bulge test. In: AIP Conference Proceedings. 1353, AIP Publishing, pp. 1429–1434. http://dx.doi.org/10.1063/1.3589717.

Machado, G., Favier, D., Chagnon, G., 2012. Membrane curvatures and stress-strain full fields of axisymmetric bulge tests from 3D-DIC measurements. Theory and validation on virtual and experimental results. Exp. Mech. 52 (7), 865–880. http://dx.doi.org/10.1007/s11340-011-9571-3.

Maeno, T., Mori, K.-i., Ogihara, T., Fujita, T., 2018. Blanking immediately after heating and ultrasonic cleaning for compact hot-stamping systems using rapid resistance heating. Int. J. Adv. Manuf. Technol. 97 (9), 3827–3837. http://dx.doi.org/10.1007/s00170-018-2232-2.

Maeno, T., Mori, K.-i., Ogihara, T., Fujita, T., 2019. Removal of thin oxide scale by ultrasonic cleaning with diluted hydrochloric acid in hot stamping of bare 22MnB5 sheet using resistance heating. Procedia Manuf. 29, 225–231. http://dx.doi.org/10.1016/j.promfg.2019.02.130.

Maeno, T., Mori, K.-i., Sakagami, M., Nakao, Y., Talebi-Anaraki, A., 2020. Minimisation of heating time for full hardening in hot stamping using direct resistance heating. J. Manuf. Mater. Process. 4 (3), http://dx.doi.org/10.3390/jmmp4030080.

Mahabunphachai, S., Koç, M., 2010. Investigations on forming of aluminum 5052 and 6061 sheet alloys at warm temperatures. Mater. Des. 31 (5), 2422–2434. http://dx.doi.org/10.1016/j.matdes.2009.11.053.

Merklein, M., Lecher, J., Gödel, V., Bruschi, S., Ghiotti, A., Turetta, A., 2007. Mechanical properties and plastic anisotropy of the quenchenable high strength steel 22MnB5 at elevated temperatures. In: Sheet Metal 2007. In: Key Engineering Materials, 344, Trans Tech Publications Ltd, pp. 79–86. http://dx.doi.org/10.4028/www.scientific.net/KEM.344.79.

Merklein, M., Lechler, J., 2006. Investigation of the thermo-mechanical properties of hot stamping steels. In: Proceedings of the 11th International Conference on Metal Forming 2006. J. Mater Process. Technol. 177 (1–3), 452–455. http://dx.doi.org/10.1016/j.jmatprotec.2006.03.233.

Min, J., Stoughton, T.B., Carsley, J.E., Carlson, B.E., Lin, J., Gao, X., 2017. Accurate characterization of biaxial stress-strain response of sheet metal from bulge testing. In: Advances in Metal Forming Research In Honor of Dong-Yol Yang. Int. J. Plast. 94, 192–213. http://dx.doi.org/10.1016/j.ijplas.2016.02.005.

Mori, K.-i., Abe, Y., Miyazawa, S., 2020. Warm stamping of ultra-high strength steel sheets at comparatively low temperatures using rapid resistance heating. Int. J. Adv. Manuf. Technol. 108 (11), 3885–3891. http://dx.doi.org/10.1007/s00170-020-05642-x.

Mori, K., Bariani, P.F., Behrens, B.A., Brosius, A., Bruschi, S., Maeno, T., Merklein, M., Yanagimoto, J., 2017. Hot stamping of ultra-high strength steel parts. CIRP Ann. 66 (2), 755–777. http://dx.doi.org/10.1016/j.cirp.2017.05.007.

Mori, K., Maki, S., Tanaka, Y., 2005. Warm and hot stamping of ultra high tensile strength steel sheets using resistance heating. CIRP Ann. 54 (1), 209–212. http://dx.doi.org/10.1016/S0007-8506(07)60085-7.

Mulder, J., Vegter, H., Aretz, H., Keller, S., van den Boogaard, A.H., 2015. Accurate determination of flow curves using the bulge test with optical measuring systems. J. Mater Process. Technol. 226, 169–187. http://dx.doi.org/10.1016/j.jmatprotec.2015.06.034.

Nakagawa, Y., ichiro Mori, K., Nishikata, M., 2020. Hot stamping of non-rectangular steel sheets using resistance heating by local preheating. Procedia Manuf. 50, 298–302. http://dx.doi.org/10.1016/j.promfg.2020.08.055, 18th International Conference on Metal Forming 2020.

Panknin, W., 1959. Der hydraulische Tiefungsversuch und die Ermittlung von Fließkurven (The hydraulic bulge test and the determination of the flow stress curves) (Ph.D. thesis). University of Stuttgart.

Pradille, C., Bay, F., Mocellin, K., 2010. An experimental study to determine electrical contact resistance. In: 2010 Proceedings of the 56th IEEE Holm Conference on Electrical Contacts. pp. 1–5. http://dx.doi.org/10.1109/HOLM.2010.5619522.

Ravier, P., Aranda, L.G., Chastel, Y., 2003. Hot Stamping Experiment And Numerical Simulation Of Pre-coated USIBOR1500 Quenchable Steels. pp. 2003–01–2859. http://dx.doi.org/10.4271/2003-01-2859.

Reis, L.C., Oliveira, M.C., Santos, A.D., Fernandes, J.V., 2016. On the determination of the work hardening curve using the bulge test. Int. J. Mech. Sci. 105, 158–181. http://dx.doi.org/10.1016/j.ijmecsci.2015.11.009.

Reitz, A., Grydin, O., Schaper, M., 2022. Influence of thermomechanical processing on the microstructural and mechanical properties of steel 22MnB5. Mater. Sci. Eng. A 838, 142780. http://dx.doi.org/10.1016/j.msea.2022.142780.

Rogeon, P., Raoelison, R., Carre, P., Dechalotte, F., 2008. A microscopic approach to determine electrothermal contact conditions during resistance spot welding process. J. Heat Transfer 131 (022101), http://dx.doi.org/10.1115/1.3000596.

Santos, T.G., Miranda, R.M., Vilaça, P., 2014. Friction stir welding assisted by electrical Joule effect. J. Mater Process. Technol. http://dx.doi.org/10.1016/j.jmatprotec.2014.03.012.

Sène, N.A., Balland, P., Arrieux, R., Bouabdallah, K., 2013. An experimental study of the microformability of very thin materials. Exp. Mech. 53 (2), 155–162. http://dx.doi.org/10.1007/s11340-012-9623-3.

Shao, Z., Bai, Q., Li, N., Lin, J., Shi, Z., Stanton, M., Watson, D., Dean, T., 2018. Experimental investigation of forming limit curves and deformation features in warm forming of an aluminium alloy. Proc. Inst. Mech. Eng. B 232 (3), 465–474. http://dx.doi.org/10.1177/0954405416645776.

Shao, Z., Li, N., Lin, J., Dean, T.A., 2016. Development of a new biaxial testing system for generating forming limit diagrams for sheet metals under hot stamping conditions. Exp. Mech. 56 (9), 1489–1500. http://dx.doi.org/10.1007/s11340-016-0183-9.

Suttner, S., Merklein, M., 2016. Experimental and numerical investigation of a strain rate controlled hydraulic bulge test of sheet metal. J. Mater Process. Technol. 235 (Supplement C), 121–133. http://dx.doi.org/10.1016/j.jmatprotec.2016.04.022.

Terhorst, M., Ozhoga-Maslovskaja, O., Trauth, D., Shirobokov, A., Mattfeld, P., Solf, M., Klocke, F., 2016. Electro-thermo-mechanical contact model for bulk metal forming under application of electrical resistance heating. Int. J. Adv. Manuf. Technol. 1–18. http://dx.doi.org/10.1007/s00170-016-9315-8.

Venturato, G., Novella, M., Bruschi, S., Ghiotti, A., Shivpuri, R., 2017. Effects of phase transformation in hot stamping of 22MnB5 high strength steel. In: 17th International Conference on Sheet Metal, SHEMET17. Procedia Eng. 183, 316–321. http://dx.doi.org/10.1016/j.proeng.2017.04.045.

Wang, G., Li, X., Liu, S., Gu, Y., 2018. Improved superplasticity and microstructural evolution of Ti2AlNb alloy sheet during electrically assisted superplastic gas bulging. Int. J. Adv. Manuf. Technol. http://dx.doi.org/10.1007/s00170-018-2431-x.

Wang, Z.-j., Liu, J.-g., Li, Y., 2010. Fracture prediction in non-isothermal viscous pressure bulging of aluminum alloy sheet using ductile fracture criterion. J. Central South Univ. Technol. 17 (3), 449–453. http://dx.doi.org/10.1007/s11771-010-0505-5.

Wu, Y., Liu, G., Liu, Z., Wang, B., 2016. Formability and microstructure of Ti22Al24.5Nb0.5Mo rolled sheet within hot gas bulging tests at constant equivalent strain rate. Mater. Des. 108, 298–307. http://dx.doi.org/10.1016/j.matdes.2016.06.109.